

1 **Comprehensive in-vivo secondary structure of the SARS-CoV-2 genome reveals**
2 **novel regulatory motifs and mechanisms**

3
4 Nicholas C. Huston,^{1*} Han Wan,^{2*} Rafael de Cesaris Araujo Tavares,³ Craig Wilen,^{4,5} Anna Marie
5 Pyle^{2,3,6,#}
6

7 ¹Department of Molecular Biophysics and Biochemistry, Yale University, New Haven, CT, USA

8 ²Department of Molecular, Cellular, and Developmental Biology, Yale University, New Haven, CT, USA

9 ³Department of Chemistry, Yale University, New Haven, CT, USA

10 ⁴Department of Laboratory Medicine, Yale School of Medicine, New Haven, CT, USA

11 ⁵Department of Immunobiology, Yale School of Medicine, New Haven, CT, USA

12 ⁶Howard Hughes Medical Institute, Chevy Chase, MD, USA

13 Running Head: Complete *in-vivo* SHAPE-MaP structure of the SARS-CoV-2 genome

14 #Address correspondence to Anna Marie Pyle, anna.pyle@yale.edu

15 *Nicholas C. Huston and Han Wan contributed equally to this work. Nicholas C. Huston is listed first
16 because he performed the large majority of experimental work.

17
18 Abstract Word Count: 249

19 Text Word Count: 8,103
20
21
22
23
24

25 **Summary**

26 SARS-CoV-2 is the positive-sense RNA virus that causes COVID-19, a disease that has
27 triggered a major human health and economic crisis. The genome of SARS-CoV-2 is unique among
28 viral RNAs in its vast potential to form stable RNA structures and yet, as much as 97% of its 30
29 kilobases have not been structurally explored in the context of a viral infection. Our limited knowledge
30 of SARS-CoV-2 genomic architecture is a fundamental limitation to both our mechanistic understanding
31 of coronavirus life cycle and the development of COVID-19 RNA-based therapeutics. Here, we apply a
32 novel long amplicon strategy to determine for the first time the secondary structure of the SARS-CoV-2
33 RNA genome probed in infected cells. In addition to the conserved structural motifs at the viral termini,
34 we report new structural features like a conformationally flexible programmed ribosomal frameshifting
35 pseudoknot, and a host of novel RNA structures, each of which highlights the importance of studying
36 viral structures in their native genomic context. Our in-depth structural analysis reveals extensive
37 networks of well-folded RNA structures throughout Orf1ab and reveals new aspects of SARS-CoV-2
38 genome architecture that distinguish it from other single-stranded, positive-sense RNA viruses.
39 Evolutionary analysis of RNA structures in SARS-CoV-2 shows that several features of its genomic
40 structure are conserved across beta coronaviruses and we pinpoint individual regions of well-folded
41 RNA structure that merit downstream functional analysis. The native, complete secondary structure of
42 SAR-CoV-2 presented here is a roadmap that will facilitate focused studies on mechanisms of
43 replication, translation and packaging, and guide the identification of new RNA drug targets against
44 COVID-19.

45

46

47

48

49

50 INTRODUCTION

51 Severe acute respiratory syndrome related coronavirus 2 (SARS-CoV2), which is responsible for the
52 current global pandemic(Zhu et al., 2020), is a positive strand RNA virus in the genus *β-coronavirus*. To
53 date, the outbreak of SARS-CoV2 has infected at least 12 million people globally, causing great
54 economic loss and posing an ongoing public health threat(Dong et al., 2020). Included in the *β*-
55 coronavirus genus are two related viruses, SARS-CoV and Middle East respiratory syndrome
56 coronavirus (MERS-CoV), that caused global outbreaks in 2003 and 2012, respectively(de Wit et al.,
57 2016). Despite the continued risk posed by *β*-coronaviruses, mechanistic studies of the family are
58 limited and to date no effective antivirals or vaccines exist, highlighting the need for research that
59 facilitates the development of therapeutics. With most research efforts focusing on viral proteins (Lan et
60 al., 2020a, Yin et al., 2020, Wan et al., 2020), little is known about the viral RNA genome, especially its
61 structural content. This is a major gap in our understanding because RNA structural elements in
62 positive strand viruses play central roles in regulating all aspects of replication, translation, packaging
63 and host defense (McMullan et al., 2007, Fricke et al., 2015, Pirakitikulr et al., 2016, Clyde and Harris,
64 2006, MacFadden et al., 2018), so an understanding of their location and function is critical for
65 mechanistic understanding and strategies for viral control(Barrows et al., 2018, Adams et al., 2017).
66 Given the success of antimicrobials targeted against conserved RNA structural elements in other
67 pathogen genomes(Warner et al., 2018, Fedorova et al., 2018), there is an urgent, unmet need to
68 elucidate the genome architecture of SARS-CoV-2.

69 Like other coronaviruses, the genome of SARS-CoV-2 is incredibly large (Maier et al., 2015, Zhu et
70 al., 2020). Two open reading frames (ORF) for viral nonstructural proteins (Nsp) and 9 small ORFs that
71 encode the structural proteins and a number of accessory genes comprise a ~30kb genome(Kim et al.,
72 2020). These ORFs are flanked on either side by a 5' and 3'UTR that have been shown in other
73 coronaviruses to possess conserved RNA structures with important functional roles in the viral life
74 cycle(Yang and Leibowitz, 2015). Studies in Murine Hepatitis Virus (MHV) and Bovine Coronavirus
75 (BCoV) suggest that the 5' viral termini folds in to 6 stems (SL1-SL6) that play roles in sgRNA synthesis

76 and viral replication(Madhugiri et al., 2018, Chen and Olsthoorn, 2010). In the 3'UTR, a pseudoknot
77 and a bulged stem loop (BSL) are essential for sgRNA synthesis in MHV(Zust et al., 2008).

78 One of the best-studied functional RNA elements in β -coronavirus genomes is the programmed
79 ribosomal frameshifting pseudoknot (PRF) that sits at the boundary between Orf1a and Orf1ab(Plant
80 and Dinman, 2008). The PRF, found in all coronaviruses, induces a -1 ribosomal frameshift that allows
81 for bypassing of the Orf1a stop codon and production of the orf1ab polyprotein, which includes the viral
82 replicase(Plant et al., 2005). Reporter assays using a truncated PRF construct showed that
83 programmed frameshifting occurs ~25% of the time in SARS-CoV(Kelly et al., 2020), and that it is
84 crucial for sgRNA synthesis(Plant et al., 2013). Extensive mutational analysis has revealed a three-
85 stemmed pseudoknot structure for the SARS-CoV PRF(Plant et al., 2005). However, neither the
86 mechanism of frameshifting regulation nor the three-stem pseudoknot PRF conformation has been
87 validated in cells.

88 While recent computational studies suggest the 5'UTR, 3'UTR, and PRF functional elements
89 are conserved in the SARS-CoV-2 genome(Rangan et al., 2020, Andrews et al., 2020), these regions
90 account for a vanishingly small fraction of the total nucleotide content. Studies of other positive-sense
91 viral RNA genomes such as Hepatitis C virus (HCV) and Human Immunodeficiency Virus (HIV) have
92 revealed extensive networks of regulatory RNA structures contained within viral ORFs(Siegfried et al.,
93 2014, Pirakitikulr et al., 2016, Friebe and Bartenschlager, 2009, Li et al., 2018, You et al., 2004) which
94 direct critical aspects of viral function. It is therefore of crucial importance to assess and characterize
95 the structural features of the SARS-CoV-2 ORF, as elucidation of structural motifs will improve our
96 understanding of all coronaviruses and facilitate development of antiviral therapies for the entire family.

97 Recent advances in high-throughput structure probing methods (SHAPE-MaP, DMS-MaP) have
98 greatly facilitated the structural studies of long viral RNAs (Siegfried et al., 2014, Zubradt et al., 2017).
99 Recently, Manfredonia et al. performed full-length SHAPE-MaP analysis on *ex vivo* extracted and
100 refolded SARS-CoV-2 RNA(Manfredonia et al., 2020). However, structural studies on both viral and
101 messenger RNA have highlighted the importance of probing RNAs in their natural cellular

102 context(Simon et al., 2019, Rouskin et al., 2014). Lan et al performed full-length *in-vivo* DMS-MaPseq
103 on SARS-CoV2 infected cells(Lan et al., 2020b), but as DMS only reports on A and C nucleotides, the
104 data coverage is necessarily sparse. While both studies reveal important features of the structural
105 content in the SARS-CoV-2 genome and its evolutionary conservation, to date no work has been
106 published that captures information for every single nucleotide in an *in-vivo* context.

107 Here, we report for the first time the complete secondary structure of SARS-CoV-2 RNA
108 genome using in SHAPE-MaP data obtained in living cells. We deploy a novel long amplicon method
109 readily adapted to other long viral RNAs made possible by the highly processive reverse transcriptase
110 MarathonRT (Guo et al., 2020). The resulting genomic secondary structure map reveals functional
111 motifs at the viral termini that are structurally homologous to other coronaviruses, thereby fast-tracking
112 our understanding of the SARS-CoV-2 life cycle. We reveal conformational variability in the PRF,
113 highlighting the importance of studying viral structures in their native genomic context and underscoring
114 their dynamic nature. We also uncover elaborate networks of well-folded RNA structures dispersed
115 across Orf1ab, and we reveal features of the SARS-CoV-2 genome architecture that distinguish it from
116 other single-stranded, positive-sense RNA viruses. The analysis reveals large RNA structures within
117 the ORF that may ultimately prove to be as important for viral function as the PRF. Evolutionary
118 analysis of the full-length SARS-CoV-2 structure suggests that, not only do its architectural features
119 appear to be conserved across the β -coronavirus family, but individual regions of well-folded RNA may
120 be as well. Our work reveals the unique genomic architecture of SARS-CoV-2 in infected cells, points to
121 important viral strategies for infection and persistence, and identifies potential drug targets. The full-
122 length structure model we present here thus serves as an invaluable roadmap for future studies on
123 SARS-CoV-2 and other coronaviruses that emerge in the future.

124

125 **Keywords**

126 SARS-CoV-2, RNA genome architecture, *in-vivo* SHAPE-MaP, Functional RNA structure

127

128 **MATERIALS & METHODS**

129 **Cell Culture and SARS-CoV-2 Infection**

130 VeroE6 cells were cultured in Dulbecco's Modified Eagle Medium (DMEM) with 10% heat-
131 inactivated fetal bovine serum (FBS). Approximately 5×10^6 cells were plated in each of four T150 tissue
132 culture treated flasks. The following day media was removed and 10^5 PFU in 4mL of media of SARS-
133 CoV-2 isolate USA-WA1/2020 (BEI Resources #NR-52281) was added to each flask. Virus was
134 adsorbed for 1 hour at 37°C and then 16mL of fresh media was added to each flask.

135

136 **RNA Probing and Purification**

137 Four days post-infection (dpi), the supernatant was aspirated from each flask, cells were
138 washed with 10mL of cold PBS^{-/-} and then dislodged in 10ml PBS^{-/-} with a cell scraper. The contents
139 were collected and centrifuged at 450g x 5 min at 4°C. The supernatant was removed and the cell
140 pellet was resuspended into 2ml of PBS^{-/-} with 200µl DMSO or 2ml PBS with 200µl of 2M NAI (final
141 concentration = 200mM). Cells were incubated for 10 minutes at room temperature followed by
142 addition of 6mL of Trizol. RNA was extracted with the addition of 1.2mL of chloroform. The aqueous
143 phase was transferred to a new tube, followed by the addition of 12mL of 100% EtOH (70% final) and
144 precipitated overnight at -20°C. RNA was resuspended in 1xME buffer and purified using the Qiagen
145 RNeasy kit according to the manufacturer's protocol. RNA was eluted in 1xME buffer.

146

147 **Tiled-Amplicon Design**

148 Leveraging the extreme processivity of MarathonRT, a highly processive group II intron-
149 encoded RT(2), we designed fifteen 2000nt amplicon and a single 1300nt amplicons tiled across the
150 SARS-CoV-2 genome for full sequencing coverage. Adjacent amplicons were designed with a 100nt
151 overlap to ensure data is collected for regions otherwise masked by primer binding. Primers for reverse
152 transcription (RT) were designed using the OligoWalk tool(Lu and Mathews, 2008) to avoid highly-
153 structured primers and highly-structured regions of the SARS-CoV-2 genome. Forward and reverse

154 primer sets were designed for an optimal T_m of 58°C. Reverse primers were inset 3nt from the 5'end of
155 the RT primer to enhance specificity of the PCR reaction.

156

157 **Reverse Transcription with MarathonRT**

158 MarathonRT purification was performed as described in (Guo et al., 2020). For each amplicon,
159 500ng of total cellular RNA was mixed with 1µL of the corresponding 1µM RT primer. Gene-specific
160 primers used for RT are listed in **Table S2**. Primers were annealed at 65°C for 5min then cooled to
161 room temperature, followed by addition of 8µL of 2.5x MarathonRT SHAPE-Map Buffer (125mM 1M
162 Tris-HCl pH 7.5, 500mM KCl, 12.5mM DTT, 1.25mM dNTPs, 2.5mM Mn^{2+}), 4µL of 100% glycerol, and
163 0.5µL of MarathonRT. RT reactions were incubated at 42°C for 3 hours. 1µL 3M NaOH was added to
164 each reaction and incubated at 95°C for 5min to degrade the RNA, followed by the addition of 1µL 3M
165 HCl to neutralize the reaction. cDNA was purified using AmpureXP beads (Cat. No. A63880) according
166 to manufacturer's protocol and a 1.8x bead-to-sample ratio. Purified cDNA was eluted in 10µL
167 nuclease-free water.

168

169 **SHAPE-MaP Library Construction**

170 Amplicons tiling the SARS-CoV-2 genome were generated using NEBNext UltraII Q5 MasterMix
171 (Cat. No. M0544L), gene-specific forward and reverse PCR primers, and 5µL of purified cDNA. Gene-
172 specific primers used for PCR are listed in **Table S3**. Touchdown cycling PCR conditions were used to
173 enhance PCR specificity (68-58°C annealing temperature gradient). PCR reaction products were
174 purified with Monarch DNA Clean-up Kits (NEB) with a binding buffer:sample ratio of 2:1 to remove
175 products smaller than 2kb. PCR products were visualized on 0.8% agarose gels to confirm production
176 of correctly sized amplicons. Amplicons were diluted to 0.2ng/µL and then pooled into two odd and two
177 even amplicon pools for downstream library preparation. Sequencing libraries were generated using a
178 NexteraXT DNA Library Preparation Kit (Illumina) according to manufacturer's protocol, but with 1/5th
179 the recommended volume. Libraries were quantified using a Qubit (Life Technologies) and a

180 BioAnalyzer (Agilent). Amplicon pools were recombined and sequenced on a NextSeq 500/550
181 platform using a 150 cycle mid-output kit.

182

183 **Structure Prediction**

184 All libraries were analyzed using ShapeMapper 2(Busan and Weeks, 2018), aligning reads to
185 SARS-CoV-2 genome (accession number: MN908947). Mutation rates between NAI-modified and
186 unmodified samples were tested for significance using the equal variance t-test. Using reactivities
187 output from ShapeMapper, ShapeKnots(Hajdin et al., 2013) was used to determine whether two
188 previously reported pseudoknots contained in the SARS-CoV-2 genome were predicted with
189 experimental SHAPE constraints. The two pseudoknots tested were the programmed ribosomal
190 frameshifting element that exists at the Orf1a/b boundary, and a pseudoknot in the 3'UTR that was
191 identified in the MHV and B-CoV genomes (references). We analyzed all 500nt windows separated by
192 a 100nt slide that contained each of the putative pseudoknots to determine if the pseudoknot was
193 successfully predicted.

194 SuperFold (Smola et al., 2015b) was used to generate a consensus structure prediction for the
195 entire SARS-CoV-2 genome using SHAPE reactivities obtained from biological replicate 1 as
196 constraints. We imposed a maximum pairing distance of 500nt. As our data only supported formation of
197 the pseudoknot contained in the programmed ribosomal frameshifting element, only this pseudoknot
198 was forced in this prediction. All structures output from the SuperFold prediction were visualized and
199 drawn using StructureEditor, a tool in the RNAStructure software suite(Reuter and Mathews, 2010).

200 Base-pairing distances were calculated from .ct structure files output from SuperFold full-length
201 SARS-CoV-2 consensus predictions, and compared to previously published, publically available full-
202 length genome structures for Dengue and Hepatitis C Virus generated with SHAPE constraints, a max-
203 pairing distance of 500nt, and the SuperFold pipeline (Mauger et al., 2015, Dethoff et al., 2018).

204

205 **Identification of Well-Folded Regions**

206 Two data signatures were used to identify well-folded regions: The first is the SHAPE reactivity
207 data generated with the SHAPE-MaP workflow and the ShapeMapper analysis tool(Busan and Weeks,
208 2018). The second is the Shannon entropy calculated from base-pairing probabilities determined during
209 the SuperFold partition function calculation(Smola et al., 2015b). Two replicate data sets were used,
210 including separate SuperFold predictions.

211 Local median SHAPE reactivity and Shannon Entropy were calculated in 55nt sliding windows.
212 The global median SHAPE reactivity or Shannon Entropy were subtracted from calculated values to aid
213 in data visualization. Regions with local SHAPE and Shannon Entropy signals 1) below the global
214 median 2) for stretches longer than 40 nucleotides 3) that appear in both replicate data sets were
215 considered well-folded. Disruptions, or regions where local SHAPE or Shannon Entropy rose above the
216 global median, are not considered to disqualify well-folded regions if they extended for less than 40
217 nucleotides. Arc plots generated from each replicate consensus structure prediction were compared
218 for regions that meet sorting criteria described above in order to ensure agreement between secondary
219 structure models generated from each replicate SHAPE-MaP dataset.

220 Base-pairing distances of well-folded regions were calculated from .ct structure files output from
221 SuperFold consensus predictions, and compared to previously published, publicly available structures
222 for well-folded regions of the HIV genome generated with SHAPE constraints, a max-pairing distance of
223 500nt, and the SuperFold pipeline (Siegfried et al., 2014).

224

225 **Multiple sequence alignment**

226 To analyze evolutionary support for our consensus secondary structure prediction of the SARS-
227 CoV-2 genome, we generated two codon-based multiple sequence alignments (MSA) for Orf1a and
228 Orf1b constructed from genomes of closely related viral species (Douzery EJP,2018). All sequences
229 were chosen based on a phylogenetic study of SARS-CoV-2 (Ceraolo and Giorgi, 2020). All sequences
230 referenced below were downloaded from the NCBI Taxonomy browser(Benson et al., 2018).

231 A sarbecovirus MSA was generated using SARS-CoV-2 isolate Wuhan-Hu-1 (MN908947.3),
232 four bat coronaviruses (MG772934.1, JX993987.1, DQ022305.2, DQ648857.1), and five human SARS
233 coronaviruses (AY515512.1, AY274119.3, NC_004718.3, GU553363.1, DQ182595.1).

234 We also generated an “All β -coronavirus Alignment” using the sarbecovirus sequences
235 described above in addition to four MERS-CoV sequences (MK129253, KP209307, MF598594,
236 MG987420), one HKU-4 sequence (MH002337), three HKU-5 sequence (MH002342, NC009020,
237 MH002341), four HKU1 sequences (KY674942, KF686343, AY597011, DQ415903), three murine
238 hepatitis virus sequences (AY700211, AF208067, AB551247), three human coronavirus OC43
239 sequences (AY585229, NC006213, MN026164), two bovine coronavirus sequences (KU558922,
240 KU558923), and one camel coronavirus sequence (MN514966).

241 The orf1a and orf1b region were extracted from the full-length sequences based on the
242 GenBank annotation. Separate codon alignments for both Orf1a and orf1b were generated using
243 MACSE v2.0.3(Ranwez et al., 2018) and default parameters (*-prog alignSequences*).

244

245 **Synonymous mutation rate analysis**

246 All codon alignments were visualized and edited using Jalview v 2.11.0(Waterhouse et al.,
247 2009). Synonymous mutation rates for each codon were estimated using the phylogenetic-based
248 parametric maximum likelihood (FUBAR) method(Murrell et al., 2013). Each codon was categorized as
249 base-paired or unpaired depending on strandedness of the nucleotide at the third position of each
250 codon in our SARS-CoV-2 consensus structure model(Dethoff et al., 2018). The significance of
251 synonymous mutation rates between single- and double-stranded regions was determined using two-
252 tailed, equal variance *t*-test.

253

254 **Covariation analysis**

255 Covariation calculation and visualization was performed using R-chie(Lai et al., 2012). The
256 Sarbecovirus codon alignment described above was used for covariation analysis. Identification of

257 base-pairs with statistically significant evidence of covariation was performed on individual structures
258 using R-Scape (version 0.2.1)(Rivas et al., 2017) with the RAFSp statistics by using the "--RAFSp"
259 flag(default E-value:0.05)(Tavares et al., 2019).

260

261 **Data Availability**

262 All ShapeMapper outputs, secondary structure files, and multiple sequence alignments use in this work
263 are available at the GitHub repository: [https://github.com/pylelab/SARS-CoV-](https://github.com/pylelab/SARS-CoV-2_SHAPE_MaP_structure)
264 [2_SHAPE_MaP_structure](https://github.com/pylelab/SARS-CoV-2_SHAPE_MaP_structure)

265

266

267 **RESULTS**

268 ***In-vivo* SHAPE-MaP workflow yields high quality data suitable for structure prediction.**

269 To study the SARS-CoV-2 structure in the context of infected cells, the SARS-CoV-2 isolate
270 USA-WA1/2020, isolated from an oropharyngeal swab from a patient who had returned to the United
271 States from China and developed clinical disease, was used to infect VeroE6 cells (BEI Resources
272 #NR-52281). Infection was allowed to proceed for four days, at which point cells were collected and
273 treated with either NAI or DMSO. RNA was then extracted and purified. To generate sequencing
274 libraries, 2000 nucleotide (nt) overlapping amplicons were tiled across the entire SARS-CoV-2 genome
275 (**Fig. 1A**). Importantly, this approach is made possible by the utilization of the ultra-high processive
276 reverse transcriptase MarathonRT, which encodes NAI adducts as cDNA mutations during long-
277 amplicon SHAPE-MaP library construction(Guo et al., 2020). Specifically, gene-specific primers were
278 used to prime reverse transcription in the presence of manganese, followed by amplicon PCR with
279 gene-specific primers and cycling conditions designed to enhance specificity(Korbie and Mattick, 2008).
280 Gel electrophoresis confirmed successful amplification of all 16 amplicons (data not shown).
281 Sequencing of SHAPE-MaP libraries was performed using the Illumina NextSeq 500/550 platform.

282 After generating two independent biological replicates, the resulting sequencing data were
283 analyzed using the ShapeMapper pipeline(Smola et al., 2015b). Comprehensive datasets were
284 obtained, with median effective read depth > 70,000x and effective reactivity data for 99.7%
285 (29813/29903) of nucleotides in the SARS-CoV-2 genome in both replicate experiments. To check the
286 SHAPE-MaP data quality, we analyzed the relative mutation rates of NAI-treated and DMSO-treated
287 RNA samples, revealing a significant elevation of mutation rates for NAI-treated samples (**Fig. 1B**, p-
288 value < 0.0001). This confirms that the full-length SARS-CoV-2 RNA was successfully modified *in-vivo*
289 and that these modifications were encoded as cDNA mutations.

290 To understand the relative SHAPE reactivity agreement within local regions of the genome, we
291 calculated Pearson correlation coefficients between two biological replicates. The Pearson's correlation
292 across the entire span of Orf1ab is 0.62, consistent with those previously reported for reactivities
293 calculated from *in-vivo* modified RNAs of this size(Smola et al., 2016). Across the sub genomic RNA
294 ORFs, the Pearson 's correlation is poor. We believe this reflects the fact that Amplicons 13, 14, 15,
295 and 16 will amplify both full-length *and* sub-genomic RNAs, and the difference in context will result in
296 different secondary structures(Tavares et al., 2020). For this reason, despite the fact all data have been
297 obtained globally, subsequent discrete structural analysis will focus on shared features of the viral
298 termini and the Orf1ab region.

299

300 ***De novo* structure prediction on full-length SARS-CoV-2 RNA identifies conserved functional**

301 **elements at the 5' and 3' genomic termini**

302 We performed secondary structure prediction with the SuperFold pipeline(Smola et al., 2015b),
303 using the *in-vivo* SHAPE reactivities to generate an experimentally constrained consensus secondary
304 structure prediction for the entire SARS-CoV-2 genome. As an extensive body of research has
305 elucidated structured RNA elements at the 5' and 3' viral termini as well as the Orf1ab boundary, with
306 conserved functions across β -coronaviruses, we first examined these regions from our consensus

307 prediction to determine whether they were stably folded and well-determined in the SARS-CoV-2
308 genome.

309 The 5' genomic terminus includes seven regions that have been identified and studied in other
310 coronaviruses (Reviewed in (Yang and Leibowitz, 2015)). While sequence conservation suggested that
311 these elements might be conserved in SARS-CoV-2, our consensus structure prediction shows this to
312 be the case, and we derived a specific experimentally-determined structure for this section of the
313 genome. The in-vivo SHAPE reactivity data correspond well with the resulting structural model (**Fig 2A,**
314 **inset**) and the low overall Shannon entropy values in this region (determined from base pair probability
315 calculation during the SuperFold prediction pipeline(Smola et al., 2015b)) support a well-determined
316 structure for the 5' genomic terminus ($\text{median}_{\text{Nuc}(1-400)} = 2.7 \times 10^{-5}$; global median = 0.022).

317 Individual features that typify coronavirus structures are evident in the secondary structure of
318 the SARS-CoV-2 5'-UTR with good SHAPE reactivity agreement (**Fig 2A**, inset). For example, we
319 observe a bipartite domain architecture for SL1, which was previously reported to play a role in
320 coronavirus replication(Li et al., 2008) (**Fig 2A**, labeled SL1). Similarity between SL1 structures
321 reported for other coronaviruses and the experimentally-determined structure reported here for SARS-
322 CoV-2 suggests that SL1 plays a similar role in SARS-CoV-2 life cycle.

323 Structural studies of SARS-CoV SL2 have shown that the SL2 pentaloop is stacked atop a 5-bp
324 stem. In addition, the pentaloop adopts a canonical CUYG fold in which the uracil is flipped out,
325 resulting in an architecture that is important for sgRNA synthesis(Lee et al., 2011). Our experimentally-
326 determined structure of SL2 from SARS-CoV-2 shows that it adopts exactly the same RNA fold (**Fig 2A**,
327 labeled SL2), again suggesting that it plays the same functional role in the SARS-CoV-2 life cycle.

328 The transcription regulatory sequence (TRS) is a conserved feature of β -coronaviruses and it is
329 required for sgRNA production(Yang and Leibowitz, 2015). The SARS-CoV leader TRS is predicted *in*
330 *silico* to be in stem loop 3 (SL3), with nucleotides exposed in its loop and base-paired in the stem(Chen
331 and Olsthoorn, 2010). The primary sequence of the SARS-CoV leader TRS is absolutely conserved
332 between SARS-CoV and SARS-CoV-2(Chen and Olsthoorn, 2010) (5'-ACGAAC-3'). Importantly, our

333 consensus prediction shows the SARS-CoV-2 leader TRS is also found in SL3, with a similar structural
334 organization as reported for other viruses (**Fig 2A**, labeled SL3, TRS indicated with solid black line).

335 The SL4 of SARS-CoV-2 adopts a bipartite domain structure (**Fig 2A**, labeled SL4a, SL4b)
336 similar to that reported for MHV(Kang et al., 2006, Yang et al., 2015). Importantly, the AUG of the
337 predicted upstream ORF(uORF), which is phylogenetically conserved among β -coronaviruses(Raman
338 et al., 2003), is found in the top-most stem loop of SL4a, meaning it would be accessible for recognition
339 by a scanning ribosome (**Fig 2A**, uORF start codon indicated with solid grey line).

340 As predicted across coronaviruses(Chen and Olsthoorn, 2010), the trifurcated stem at the top of
341 SL5 is observed in the experimentally-determined structure of SARS-CoV-2 (**Fig 2A**, labeled SL5A-C).
342 This includes UUCGU pentaloop motifs in SL5A and SL5B, and a GNRA tetraloop in SLC. Previous
343 reports suggest this may represent a packaging signal for GroupIIb CoVs(Chen and Olsthoorn, 2010).

344 SL6 and SL7 are predicted in the SARS-CoV-2 structure, and the in-vivo SHAPE data agree
345 strongly support the existence of these stems (**Fig 2A**, labeled SL6 and SL7). However, functional
346 evidence for SL6 and SL7 is lacking in the literature for any coronavirus.

347 The 3' genomic terminus includes three well-studied stems, including the bulged-stem loop
348 (BSL), Stem Loop 1 (SLI), and a long-bulge stem that includes the hypervariable-region (HVR), the
349 S2M domain, the octanucleotide motif (ONM) subdomains, and a pseudoknot (Reviewed in (Yang and
350 Leibowitz, 2015)). The consensus structure recapitulates the secondary structure of all the three stems
351 with good SHAPE reactivity agreement (**Fig 2B, inset**) and overall low Shannon entropy
352 ($\text{median}_{\text{Nuc}(29,472-29,870)} = 0.016$; global median = 0.022). While the BSL is well determined in our
353 structure, the low reactivity for bulged nucleotides suggests the possibility of protein binding-partners
354 (**Fig 2B**, labeled BSL).

355 A pseudoknot structure is proposed to exist between the base of the BSL stem loop and the
356 loop of SL1 in coronaviruses(Yang and Leibowitz, 2015). While pseudoknot formation is mutually
357 exclusive with the base of the BSL, studies in MHV have suggested that both structures contribute to
358 viral replication and the mutually exclusive structures are thought to function as a molecular switch in

359 different steps of RNA synthesis(Goebel et al., 2004). However, our *in-vivo* determined secondary
360 structure is inconsistent with formation of the pseudoknot (**Fig 2B**, putative base-pairing interactions
361 indicated by black lines). The low SHAPE reactivities for the nucleotides at the base of the BSL support
362 formation of the extended BSL stem, while high-reactivities of the nucleotides in the loop of SLI indicate
363 that it is highly accessible. Using the SHAPEKnots program for robust predication of pseudoknots
364 (implemented in RNA structure v5.8(Hajdin et al., 2013)), we found that a pseudoknot is never
365 predicted in three 500nt windows that cover the pseudoknotted region. Taken together, our data
366 strongly support the extended BSL conformation, indicating it is probably the dominant conformation *in-*
367 *vivo*.

368 The third stem in the 3' UTR includes three sub-domains. The HVR, so-named because it is
369 poorly conserved across group II coronaviruses(Goebel et al., 2007), is predicted to be mostly single-
370 stranded in our secondary structure, and the high reactivities across the span of this region lends
371 strong experimental support for an unstructured region (**Fig. 2B**, region indicated with solid black line
372 and labeled HVR). The fact that this region is highly unstructured may also explain why it has been
373 experimentally demonstrated to tolerate numerous deletions, rearrangements, and point mutations in
374 MHV(Goebel et al., 2007).

375 The S2M region is contained within the apical part of the third stem. We observe that the first
376 three helices of S2M from SARS-CoV-2 exactly match the crystal structure determined for S2M from
377 SARS-CoV (Robertson et al., 2005). However, our *in-vivo* structure deviates significantly at the top of
378 the stem, with bases that are highly reactive (**Fig. 2B**, region indicated with solid black line and labeled
379 S2M). It is possible that the SARS-CoV-2 S2M folds into a unique S2M conformation despite differing
380 by only a two bases (**Fig. 2B**, base-changes indicated by arrows; SARS-CoV base identity shown in
381 red). Indeed, as both single-nucleotide changes are transversions, any base-pairing interaction
382 involving these nucleotides in the SARS-CoV S2M structure could not be maintained in SARS-CoV-2.
383 Alternatively, this site could interact with factors *in-vivo* that are not captured in the crystallographic
384 study.

385 The ONM is predicted at the central bulge between the S2M region and the HVR region. The
386 sequence is absolutely conserved across β -coronavirus(Goebel et al., 2007), but no functional
387 significance has yet been shown. In our consensus structure, it is single-stranded (**Fig. 2B**, ONM
388 indicated with solid black line and labeled ONM).

389 Finally, we predict a completely different structure for the downstream terminal stem in the viral
390 3'UTR region (adjacent to the poly-A tail) than previously reported for other coronaviruses(Zust et al.,
391 2008). However, our structure prediction in this region is not highly accurate because of proximity of the
392 primer binding site. That said, the putative stem is predicted to have high Shannon entropy
393 ($\text{median}_{\text{Nuc}(29472-29495,29853-29870)} = 0.2154$; global median = 0.022), suggesting that it is not a well-ordered
394 structure in the cellular environment.

395

396 **Structure prediction of the programmed ribosomal frame-shifting element reveals**

397 **conformational flexibility**

398 One of the most well-studied RNA structures in the coronavirus coding region is the
399 programmed frame-shifting pseudoknot (PRF). It is located between orf1a and orf1b and plays an
400 important role in inducing a -1 frameshift in a translating ribosome, resulting in the synthesis of the
401 polyprotein ab, which includes the SARS-CoV-2 replicase (Plant and Dinman, 2008).

402 The PRF element previously characterized in SARS-CoV is proposed to contain three parts: an
403 attenuator stem loop, a conserved heptanucleotide “slippery” sequence, and a H-type pseudoknot
404 (Plant and Dinman, 2008). We performed SHAPEKnots(Hajdin et al., 2013) over four 500nt windows
405 that cover the pseudoknotted region in the SARS-CoV-2 genome to check if the PRF pseudoknot can
406 be discerned from our *vivo* SHAPE data. We found that the pseudoknot is successfully predicted in 3
407 out of 4 windows generated by ShapeKnots. Moreover, the nucleotides predicted to be involved in the
408 pseudoknotted helix have low SHAPE-reactivity (**Fig. 3A**, pseudoknot base-pairs indicated with red
409 lines). Our *in-vivo* SHAPE data therefore strongly support the formation of the pseudoknotted helix, and

410 the frame-shifting pseudoknot was thereafter included as a hard constraint during secondary structure
411 prediction.

412 The most probable, dominant structure of the PRF region, extracted from the full-length *in-vivo*
413 secondary structure, is shown in **Fig. 3A**. In our model, the SHAPE reactivity and Shannon entropy
414 calculation support a well-folded attenuator stem (AS) immediately upstream of the heptanucleotide
415 slippery sequence (HSS) (**Fig 3A**; AS and HSS indicated with labeled, solid black lines). The attenuator
416 stem has been demonstrated to be important for attenuating frameshifting in SARS-CoV(Cho et al.,
417 2013), and previous reports suggested that the attenuator stem structure is not well conserved between
418 SARS-CoV and SARS-CoV-2(Kelly et al., 2020). By contrast, our results suggest a SARS-CoV-2-
419 specific fold for the attenuator stem. The highly conserved heptanucleotide slippery sequence is
420 predicted to be single-stranded in our in-vivo structural model, which is consistent with studies on other
421 coronaviruses(Plant et al., 2005, Plant and Dinman, 2008).

422 Overall, the dominant structure prediction for the H-type pseudoknot in our structural model
423 differs from the one characterized in SARS-CoV. The H-type pseudoknot in SARS-CoV is composed of
424 three coaxially stacked stems: SL1, SL2 and the pseudoknotted helix(Plant et al., 2005). The SL1 stem,
425 which contains the upstream pseudoknotted loop, is well folded in our consensus model as indicated by
426 SHAPE reactivity mapping (**Fig. 3A**; labeled SL1) and Shannon entropy (**Fig. 3C**, $\text{median}_{\text{Nuc}(13476-13503)}$
427 $= 1.9 \times 10^{-4}$; global median = 0.022). Importantly, the region reported to contain the SL2 stem(Rangan et
428 al., 2020, Plant et al., 2005) is predicted as single-stranded in our consensus structure, and
429 consequently does not include SL2 (**Fig 3A**; region indicated by dotted black line). Rather, the
430 dominant structure predicted for the PRF includes a different stem, SL3, that includes the downstream
431 pseudoknot arm (**Fig 3A**; labeled SL3). However, neither the single-stranded region nor SL3 are well-
432 determined in our structure as indicated by Shannon entropy mapping to the region (**Fig. 3C**,
433 $\text{median}_{\text{Nuc}(13503-13534)} = 0.24$; global median = 0.022, labeled with a dotted black-line and SL3,
434 respectively).

435 As SuperFold calculates a partition function, lower probability base-pairing interactions are
436 captured during structure prediction steps. We therefore checked alternative, low probability base-pair
437 interactions captured for the PRF region. We found that the single-stranded region (**Fig. 3A**; indicated
438 by dotted black line) forms base-pairing interaction as many as 6 different regions in the SARS-CoV-2
439 genome (data not shown). We sought to determine if the previously reported SL2 conformation was
440 captured among them. Indeed, an alternate, lower probability structure containing an extended SL2 is
441 generated in the SuperFold prediction with the attenuator stem, heptanucleotide slippery sequence,
442 and SL1 intact. (**Fig. 3B**; alternate SL2 conformation labeled). In this variation, the SL2 stem is
443 predicted to fold with a median probability of 20% as determined from the probabilities of each
444 individual base-pair of the SL2 stem (**Fig. 3D**; individual base-pairs indicated with grey dots). In
445 contrast, the SL3 stem predicted in our dominant consensus structure has as much as 80% probability
446 of folding. The chemical probing data does not strongly support one structure over another (**Fig. 3A** and
447 **Fig. 3B**) and likely reflects structural flexibility and pairing promiscuity for the SL2 region. Taken
448 together, data determined *in-vivo* suggest that the frame-shifting pseudoknot in SARS-CoV-2 includes a
449 well-folded attenuator stem, SL1, and a pseudoknot, but that the region containing the putative SL2 is
450 conformationally flexible. Future studies are needed to explore if there is relationship between the
451 structural flexibility and the mechanistic role of the frameshifting pseudoknot.

452

453 **The secondary structure of SARS-CoV-2 Orf1ab reveals a network of unique RNA structural** 454 **elements**

455 While the successful identification of known, functional RNA structural elements lends strong
456 support for our methodology and for the overall secondary structural model, these known regions
457 account for only 3% of the total nucleotide content of the SARS-CoV-2 genome; little is known about
458 remaining 97%.

459 Here we report the first *in-vivo*-derived, SHAPE-constrained secondary structural model that
460 includes a description of the base-pairing interactions for all nucleotides within a coronavirus genome

461 (**Fig. 4A**; secondary structures described by arc plots underneath each of the three SHAPE/Shannon
462 plots). Representative secondary structural maps of small regions extracted from the consensus
463 prediction exemplify the types of substructures that are observed in protein-encoding regions of SARS-
464 CoV-2 (**Fig. 4B**, structures contained within Nsp3 and spanning Nsp6&7; nt4716-5682, nt11221-12043,
465 respectively). This resource is a valuable roadmap for ongoing studies, and to that end, a .ct file for the
466 full-length SARS-CoV-2 genome structure is freely available (see Data Availability).

467 To discover additional, well-folded RNA structures within the SARS-CoV-2 genome, we used a
468 sliding 55nt window to calculate the local median Shannon Entropy and we correlated these values with
469 experimentally-determined SHAPE reactivities (**Fig 4A**). Only regions with both median Shannon
470 entropy and SHAPE reactivity signals below the global median for stretches longer than 40nt, and
471 which appear in both replicate data sets, were considered well-determined and stable. In total, we
472 identify 40 such regions in Orf1ab (**Fig. 4B**, shaded). Hereafter, any structured region that meets these
473 above criteria will be referred to as “well-folded.”

474 We also identified well-folded regions in the subgenomic RNA region (data not shown).
475 However, our previous correlation analysis suggests that the SHAPE signal from this region includes
476 reactivity signals from multiple RNA species, including genomic and subgenomic RNAs. Given the
477 method deployed to construct our SHAPE-MaP sequencing libraries, it is impossible to deconvolute
478 sgRNA data from genomic data, and new approaches will be required to separate genomic from
479 subgenomic structures. While it will be interesting to explore this issue in subsequent studies, the
480 following analysis focuses on stable structures within the orf1ab region, which can be uniquely
481 determined.

482 To understand architectural organization of the overall “structuredness”, or base-pair content
483 (BPC) within orf1ab, we calculated the double-strand content of individual protein domains within this
484 region of the genome (**Fig. 5A**, grey bars). We find that all protein domains have comparable BPC, with
485 an average of 56% (+/- 6.09%) of nucleotides involved in base-pairing interactions. However, the RNA
486 sequences within each protein domain are not equivalently well-folded (**Fig 5A**, black bars). For

487 example, we observe that ~50% of nucleotides within the 5'UTR, Nsp1, Nsp6, Nsp8, and Nsp12 are
488 concentrated in well-folded regions, suggesting these domains may be hubs for regulatory RNA
489 structures. By contrast, Nsp13, Nsp14, and Nsp16 have <15% of their nucleotide content lies in
490 discretely well-folded regions. At the most extreme end, Nsp10 contains no nucleotides in well-folded
491 regions. Considering that Nsp10 is located immediately upstream of the PRF, this lack of well-folded
492 structures may be important to direct proper frameshifting.

493 While analyzing the resulting secondary structural map, we noticed that the SARS-CoV-2
494 genome contains long-stretches of short, locally-folded stem loops (for example - **Fig. 4B**) with few
495 long-distance base-pairing interactions such as those indicated by large arcs in typical arc plots (**Fig.**
496 **4A**). Wondering if this was quantifiable feature unique to the SARS-CoV-2 genome, we calculated the
497 distance between base-paired nucleotides for every base-pairing interaction in our SARS-CoV-2
498 structural model. We compared these SARS-COV-2 base-pairing distances to those we calculated from
499 published full-length structural models for HCV(Mauger et al., 2015) and Dengue Virus(Dethoff et al.,
500 2018), where the data were prepared using the same structure prediction pipeline and constraints used
501 in our study. Interestingly, the median base-pairing distance in our SARS-CoV-2 consensus model is
502 25nt, and is significantly smaller than the median base-pairing distance in the HCV (median=40nt) and
503 Dengue Virus (median=33nt) consensus models (**Fig. 5B**). Even more, the upper bound of the
504 interquartile range (IQR) that describes the distribution of base-pairing distances in Dengue and HCV
505 genomes is much higher than the same bound in the SARS-CoV-2 genome (SARS-CoV-2 75th
506 percentile = 46nt; Dengue Virus 75th Percentile = 104nt; HCV 75th percentile = 101nt). This suggests
507 SARS-CoV-2 has fewer long-distance base-pairing interactions compared to Dengue and HCV genome.

508 We also calculated the median base-pairing distance for the well-folded regions of the SARS-
509 CoV-2 genome and compared the result to well-folded regions previously identified using the same Low
510 Shannon/Low SHAPE signatures in the HIV genome(Siegfried et al., 2014). We found that although
511 there is no significant difference in the size of well-folded regions in the SARS-CoV2 and HIV genomes
512 (data not shown), the median base-pairing distance in the well-folded regions of SARS-CoV-2 (median

513 = 26nt) is significantly lower than the base-pairing distance in well-folded regions of HIV (median = 34nt)
514 (**Fig. 5C**). Similarly, the upper bound of the IQR that describes the distribution of base-pairing distances
515 in well-folded regions of the HIV genome is much higher than the same bound in SARS-CoV-2 (SARS-
516 CoV-2 75th percentile = 44nt; HIV 75th percentile = 133nt).

517 Taken together, these results suggest that the SARS-CoV-2 genome folds into more local
518 secondary structures, such as the short stem-loops in **Fig. 4B**, and contains fewer long-range base-
519 pairing interactions than observed for other positive-sense RNA viruses. Given the exceptional size of
520 the coronavirus genome (~30kb) relative to those of the positive-sense RNA viruses compared here
521 (~10kb), it is possible that the short base-pairing distance of SARS-CoV2 may carry functional
522 implications for maintaining genomic stability, preserving fidelity of translation, and evading innate
523 immune response.

524

525 **The overall structured-ness of the SARS-CoV-2 is conserved across all β -coronaviruses**

526 Synonymous mutations rates have been used previously to lend evolutionary support for well-
527 folded RNA secondary structures in other positive-sense RNA viruses(Dethoff et al., 2018, Tuplin et al.,
528 2002, Assis, 2014, Simmonds and Smith, 1999). This body of work has suggested lower synonymous
529 rates for double-stranded nucleotides when compared to single-stranded nucleotides in viral RNAs,
530 likely reflecting an evolutionary pressure to maintain base-pairing interactions of double-stranded
531 nucleotides. We therefore computed relative synonymous mutation rates to determine how evolutionary
532 pressure is applied to single- and double-stranded regions of the SARS-CoV2 genome.

533 To generate the codon-based alignment, 33 full-length genome sequences from the NCBI
534 Taxonomy database(Benson et al., 2018) were collected, including 12 SARS-CoV genomes, 8 MERS-
535 CoV genomes, and 13 more distantly related β -coronaviruses genomes. This alignment was then used
536 to calculate synonymous and non-synonymous mutation rates (dS and dN, respectively) for each codon
537 in the SARS-CoV2 orf1ab region using A Fast, Unconstrained Bayesian AppRoximation for inferring
538 selection (FUBAR) (Murrell et al., 2013). We then separated dS and dN into single- or double-stranded

539 bins as predicted in our consensus model. The strandedness of each codon was determined by the
540 strandedness at the third position of the codon (Dethoff et al., 2018).

541 In the “All β -Coronavirus” alignment, we observed a significantly lower synonymous mutation
542 rate ($p < 0.0001$) for double-stranded codons (median = 3.765; IQR = 3.034-4.978) when compared to
543 single-stranded codons (median = 4.189; IQR = 3.232 - 5.562) in our consensus model (**Fig. 6A**). In
544 contrast, there was no significant difference ($p = 0.86$) observed for non-synonymous mutation rates
545 (dN) at single- (median = 0.4535; IQR = 0.103 – 0.685) or double-stranded codons (median = 0.453;
546 IQR = 0.139 – 0.675) (**Fig. 6B**) as dN reflects changes at the amino acid level. This suggests that
547 double-stranded regions of the SARS-CoV-2 genome experience stronger selective pressure against
548 synonymous mutations than single-stranded regions, which lends support to our consensus model and
549 suggests evolutionary maintenance of the observed secondary structure. Because an all β -coronavirus
550 alignment was used, our results indicate that the structural organization and overall base-pairing
551 content of Orf1ab is a conserved feature of the β -coronavirus family.

552 When analyzing relative synonymous mutation rates within individual protein domains, we
553 observed significantly decreased synonymous mutation rates for double-stranded codons in Nsp1,
554 Nsp2, Nsp3, Nsp4, Nsp6, Nsp8, Nsp12, Nsp13, and Nsp15 (**Fig. 6C**). Consistent with this, Nsp1, Nsp6,
555 Nsp8, and Nsp12 have >50% of their nucleotides localized within well-folded regions (**Fig. 5A**, black
556 bars). Taken together, this suggests that certain protein-coding domains contain regions of RNA
557 secondary structure that are conserved across β -Coronaviruses. For example, Nsp8, which is the most
558 well folded domain in SARS-CoV-2, is likely well-folded in other β -Coronaviruses.

559 By contrast, the base pairing content of Nsp5, Nsp7, Nsp9, Nsp10, Nsp14, and Nsp16 does not
560 appear to be conserved, as there is no significant difference in synonymous mutation rates of single-
561 and double-stranded codons (**Fig. 6C**). Consistent with this, Nsp14 and Nsp16 were shown to have
562 <15% of their nucleotides in well-folded regions, while Nsp10 does not contain any well-folded
563 nucleotides (**Fig. 5A**). Not only does this analysis support the observation that these regions of RNA

564 are not well-folded in SARS-CoV-2, our data suggest these regions may not be well folded in other β -
565 Coronaviruses.

566

567 **Evolutionary analysis for individual well-folded regions of the SARS-CoV-2 genome identifies**
568 **several conserved regions**

569 To further prioritize structural elements that may have conserved functional roles in the SARS-
570 CoV2 life cycle, we next applied our synonymous mutation rate analysis to each of the 40 discrete well-
571 folded domains identified by Low Shannon/Low SHAPE signatures (**Fig. 4B, Table S1**). Four regions
572 (regions 23, 25, 34, and 36) that are well-determined based on their low median Shannon Entropy
573 values (**Table S1**) and SHAPE reactivity data showed significantly decreased synonymous mutation
574 rates at double-stranded codons when compared to single-stranded codons across the β -coronavirus
575 alignment (**Fig. 7A, 7B**). Among those structures, region 25 and 34 are found at protein domain
576 boundaries. Region 25 ends exactly at the Nsp8/9 domain boundary, while Region 34 spans the
577 Nsp12/13 boundary. Region 23, 34, and 36 (**Fig. 7C, Fig. 7E, Fig. 7F**) contain a series of stem-loops
578 with small bulges. Region 25 contains a long-range duplex that closes a clover-leaf like structure with 8
579 stem-loops radiating from a central loop (**Fig. 7D**). This hub, or multi-helix junction might represent a
580 promising drug target, as multi-helix junctions often contain binding pockets with high binding affinity
581 and selectivity for small molecules(Warner et al., 2018).

582 Within the Sarbecovirus subgenus, we were able to identify four regions (regions 15, 22, 24, 27,
583 and 30) that are well-determined in our secondary structural model (based on low median Shannon
584 Entropy (**Table S1**) and SHAPE reactivity data) with significantly decreased synonymous mutation
585 rates in double-stranded relative to single-stranded codons (**Fig. 8A, 8B**). Among these structures,
586 Region 24 contains two discrete multi-helix junctions, each with at least three stems radiating from
587 large central loops (**Fig. 8C**). Region 27, which contains a series of six stem-loops, is particularly
588 significant because it is only 100nt downstream of the PRF in Nsp12 (**Fig 8D**). Region 15, like Region
589 24, contains several well-determined long-range duplexes that segment the region into two discrete

590 multi-helix junctions (**Fig. 8E**). Region 22 contains a series of well-folded loops and it spans the Nsp5/6
591 boundary (**Fig. 8F**). Region 30 is a single stem-loop with bulges that divide the stem into distinct
592 duplexes (**Fig. 8G**)

593 To look for evolutionary evidence that directly supports conservation of specific base-pairing
594 interactions and secondary structures, we performed covariation analysis on the 5 structures that are
595 supported by Sarbecovirus-specific synonymous mutation rates. We visualized the base-pair
596 covariation levels using R-chie (Lai et al., 2012) and we used R-scape version 0.2.1 (Rivas et al., 2017)
597 with the RAFSp statistics (Tavares et al., 2019) to test the statistical significance of putatively covarying
598 base-pairs. Specifically, we identified 3 regions (15, 22, and 30) that have covariation support (**Fig. 8E-**
599 **G**). Region 15 has three significantly covarying base-pairs at the terminus of the downstream stem loop
600 (e-value < 0.05, **Fig. 8E**); Region 22 has 2 nucleotides with have one-sided variation in the most
601 upstream stem loop (e-value < 0.05, **Fig. 8F**); Region 30 has 3 covarying base-pairs at the very top of
602 the stem loop, and a single covarying pair at the bottom portion of the stem (e-value < 0.05, **Fig. 8G**).
603 Taken together, these results suggest the existence of stable, evolutionarily conserved structural
604 elements that merit subsequent functional analysis.

605

606 **Discussion**

607 Here we establish that the SARS-CoV-2 genomic RNA has an extraordinarily complex molecular
608 architecture, filled with elaborate secondary and tertiary structural features that persist in-vivo and
609 which are conserved through time, suggesting that this network of RNA secondary structural elements
610 plays a functional role in the virus lifecycle. Indeed, the SARS-CoV-2 genome contains more well-
611 determined RNA structures than any virus studied to date, suggesting that its inherent “structuredness”
612 contributes in a unique way to viral fitness. This RNA secondary structural complexity is not just
613 confined to untranslated regions of the genome, as protein-coding sections of the SARS-CoV-2 open
614 reading frame are among the most well-structured regions. Thus, as observed for HCV, coronavirus
615 reading frames experience evolutionary pressure that simultaneously shapes both protein sequence

616 and the surrounding RNA structures in which the proteins are encoded (a “code within the
617 code”)(Pirakitikulr et al., 2016). The secondary structure that we report is well-determined based on
618 available metrics in the field(Siegfried et al., 2014). It is both a roadmap for navigating the vast RNA
619 landscape in coronaviruses, and a resource for orthogonal studies by others. As such, the data
620 reported here are all publicly available for analysis and comparison by others
621 https://github.com/pylclab/SARS-CoV-2_SHAPE_MaP_structure.

622 Well-determined secondary structures of long RNA molecules are typically difficult to obtain *in-*
623 *vivo*(Mitchell et al., 2019, Leamy et al., 2016). They are usually derived from transcripts that have been
624 refolded and probed in-vitro, or from isolated cellular transcripts that have been stripped of cellular
625 components(Smola et al., 2015a, Siegfried et al., 2014). What is particularly surprising about this
626 SARS-CoV-2 study, and the high quality of the resulting secondary structure, is the fact that it was
627 entirely determined *in-vivo*, using infected cells that were treated directly with chemical probes. This
628 may be attributable to the fact that SARS-CoV-2 genomic RNA is so abundant in the infected cell,
629 ultimately becoming ~65% of the total cellular RNA(Kim et al., 2020). With so much RNA material, it
630 becomes possible to maximize the signal to noise ratio in chemical probing experiments. In addition,
631 the abundance of SARS-CoV-2 RNA may overwhelm the cell’s ability to coat transcripts with
632 nonspecific RNA binding proteins, which can otherwise limit accessibility of chemical probes. That said,
633 it will be interesting to compare the structure reported here with that obtained “*ex vivo*” (stripped of
634 protein), as that Δ SHAPE approach provides a useful way to flag possible protein binding sites(Smola
635 et al., 2015a).

636 The resulting experimental secondary structure provides new insights into known coronaviral
637 RNA motifs, and leads to the prediction of new ones that are likely to regulate viral function. The near
638 perfect structural homology of motifs at the 5’ terminus for SARS-CoV-2 and other β -coronavirus
639 genomes suggests that the function of these upstream elements is conserved in coronaviruses
640 (reviewed in (Yang and Leibowitz, 2015)). Furthermore, because our SARS-CoV-2 secondary structure

641 was determined *in-vivo*, our findings validate previous coronavirus structural models of 5'-elements, as
642 our data were obtained in a biologically relevant context.

643 Our SARS-CoV-2 secondary structure at the 3' viral terminus largely agrees with previous
644 studies on other β -coronavirus genomes (reviewed in(Yang and Leibowitz, 2015)). However, our model
645 of the 3' viral terminus deviates in one important way. Neither the raw SHAPE reactivity data nor the
646 subsequent secondary structure prediction supports formation of a pseudoknot proposed between the
647 base of the BSL and SLI. Indeed, the putative pseudoknot conformation is mutually exclusive with the
648 well-structured stem that we report at the base of the BSL. However, both conformations are proposed
649 to be essential in MHV(Goebel et al., 2004), so it is possible that the pseudoknot exists as a minority
650 conformation, or is transiently folded in SARS-CoV-2. Alternatively, because our structure represents
651 the first detailed description of a coronavirus 3'UTR structure *in-vivo*, it is possible this pseudoknot is
652 not present in other viruses.

653 Arguably the best-studied structural element in coronaviruses is the programmed ribosomal
654 frameshifting pseudoknot (PRF). Required for proper replicase translation in all coronavirus family
655 members, the PRF adopts different conformations in the various coronaviruses, including three-
656 stemmed, two-stemmed, and kissing-loop pseudoknots (Baranov et al., 2005, Plant and Dinman, 2008).
657 The core of the SARS-CoV PRF, which shares an almost identical sequence with SARS-CoV-2, is
658 predicted to form a three-stem pseudoknot comprised of SLI, SL2, and a pseudoknot helix, with an
659 additional upstream attenuator stem that is poorly conserved in SARS-CoV-2(Kelly et al., 2020). Our
660 SHAPE reactivity and structure prediction are consistent with the existence of an attenuator stem, SL1,
661 and the pseudoknot. However, our data indicate that the region corresponding to SL2 is
662 conformationally flexible, adopting an SL2 stem with only a 20% probability. Consistent with our
663 reported distribution of structural isoforms, Kelly et al. use a reporter assay to suggest that the
664 frequency of successful frameshifting in SARS-CoV-2 is about 20%(Kelly et al., 2020), indicating that
665 the observed conformational variability of SL2 may be functional. Indeed, SL2 might function like a
666 switch: When SL2 is formed (~20% of the time), frameshifting occurs. When unfolded or forming base-

667 pairs with structures outside the PRF region, frameshifting would not occur. Further studies are
668 therefore required to explore the relationship between SL2 formation and SARS-CoV-2 frame-shifting
669 efficiency.

670 The study reported here provides a structure prediction for every single nucleotide in the SARS-
671 CoV-2 genome, enabling us to simultaneously interrogate both global and local features of genome
672 architecture. One can make two major observations about the global architecture the SARS-CoV-2
673 genome. First, this *in-vivo* derived, SHAPE-constrained model strongly agrees with the high double-
674 strand RNA content predicted from the entirely *in silico* model recently reported by our lab (Tavares et
675 al., 2020). Because the data herein were obtained *in-vivo*, this work confirms that the unusually high
676 double-strand content is maintained in a cellular context. Secondly, analysis of the experimental
677 secondary structure reveals that the SARS-CoV-2 genome has a shorter median base-pairing distance
678 when compared with other positive-sense RNA viral genomes, suggesting a role for extreme
679 compaction in the function of coronaviral genomes. Downstream analysis of synonymous mutation
680 rates suggests that global architectural features are conserved across β -coronaviruses. Considering
681 the exceptional size of these genomes, the high degree of dsRNA content may represent an
682 evolutionary strategy to enhance genome stability, as duplex RNA undergoes self-hydrolysis at a much
683 slower rate than single-stranded RNA and it is more resistant to cellular nucleases(Regulski and
684 Breaker, 2008, Wan et al., 2011). Interestingly, single-stranded regions in mRNA have been shown to
685 mediate phase separation at high cellular RNA concentrations(Van Treeck et al., 2018). Because
686 SARS-CoV-2 RNA is very abundant *in-vivo* (up to 65% of total cellular RNA content (Kim et al., 2020))
687 it is possible the high dsRNA content may provide a strategy to avoid phase separation during infection.
688 The preference for abundant locally folded, short stem-loop structures in β -coronavirus genomes may
689 also provide a conserved strategy for innate immune evasion. Pattern recognition receptors such as
690 MDA5(Dias Junior et al., 2019) and ADAR modification(Nishikura, 2010) proteins recognize long RNA
691 duplexes as part of host defense processes, which could obviously be avoided by keeping duplex
692 lengths short.

693 Analysis of local features within the genome pinpoints 40 well-folded regions within the SARS-
694 CoV-2 orf1ab region. Of these 40 regions, at least five are conserved across all β -coronaviruses and
695 four are sarbecovirus specific. Four of the nine regions (Region 25, Region 34, Region 22, Region 24)
696 span boundaries between non-structural proteins, which may have relevance for polyprotein translation.
697 Previous studies have shown that RNA secondary structures can slow the rate of ribosome
698 translocation(Chen et al., 2013) and ribosome stalling is known to be important for proper folding of
699 nascent polypeptides(Collart and Weiss, 2020). Conserved, well-folded RNA structures at protein
700 domain boundaries may therefore slow or stall translocating ribosomes, thus allowing individual non-
701 structural proteins in the large Orf1a and Orf1ab poly-proteins to fold into their native conformations.

702 Intriguingly, three of the nine well-folded regions (Region 15, Region 24, Region 25) contain
703 complex, multi-helix junctions, or structural hubs. This is significant because multi-helix junctions often
704 comprise the core of RNA tertiary structures, like group II self-splicing introns, riboswitches and other
705 regulatory elements. Because these elements are likely to contain well-defined pockets, they often
706 bind specifically to small molecules, and therefore serve as possible drug targets (Warner et al., 2018,
707 Hewitt et al., 2019, Fedorova et al., 2018).

708 One important cautionary observation from our work is the poor correlation of SHAPE
709 reactivities between two *in-vivo* biological replicates for regions encoding the subgenomic RNAs.
710 Previous *in silico* work from our lab has shown that individual subgenomic RNAs (sgRNAs), such as the
711 N sgRNA, fold differently than the corresponding regions in the genomic RNA due to differences in
712 upstream sequence context(Tavares et al., 2020). Though our tiled-amplicon design affords
713 sequencing coverage for the entire SARS-CoV-2 genome, it precludes deconvolution of reactivity
714 signals for regions shared between genomic- and subgenomic RNAs. This underscores the need for
715 methodological innovations that accurately assess the structural content specific to subgenomic RNA
716 molecules. Absent such methodological advances, we caution others when interpreting reactivities
717 from the subgenomic region.

718 The *in-vivo*-determined SARS-CoV2 secondary structure present here provides a roadmap for
719 functional studies of the SARS-CoV2 genome and insights into mechanisms of the SARS-CoV-2 life
720 cycle. Evolutionary support for consensus model across β -coronaviruses hints at conserved strategies
721 for genome stability, translation fidelity, and innate immune evasion. Finally, the identification of
722 individual well-folded regions conserved across β -coronaviruses, and within the sarbecovirus subgenus,
723 provide potential targets for the study of regulatory elements, and the search for much-needed
724 therapeutically active small molecules.

725

726 **Acknowledgments**

727 We would like to thank Dr. Li-Tao Guo for preparing and sharing MarathonRT enzyme, and Dr. Ananth
728 Kumar and Gandhar Mahadeshwar (Pyle lab, Yale University) for thoughtful comments on the
729 manuscript. We would also like to thank Dr. Mark Boerneke (Weeks Lab, UNC Chapel Hill) for providing
730 data upon request. This work was supported by the Howard Hughes Medical Institute; the National
731 Institutes of Health (R01 HG009622 to A.M.P.); the NIH Grant T32AI055403 (to N.C.H.); China
732 Scholarship Council (CSC)-Yale World Scholars Program in Biomedical Sciences (to H.W.); Funding
733 for open access charge was provided by the Howard Hughes Medical Institute.

734

735 **Author Contributions**

736 N.C.H., H.W., and C.W. conducted experiments. N.C.H., H.W., C.W., and A.M.P. designed experiments.
737 N.C.H., H.W., R.C.A.T, A.M.P. wrote the paper.

738 **Declaration of Interests**

739

740 A patent application on MarathonRT has been filed by Yale University.

741

742 **Figure Legends**

743 **Figure 1.** Tiled-amplicon *in-vivo* SHAPE-MaP workflow yields high quality data for SARS-CoV-2 structure
744 prediction. **A)** Workflow of *in-vivo* SHAPE-MaP probing of full-length SARS-CoV-2 genomic RNA. **B)**
745 Mutation rates for two biological replicates confirm genomic RNA was successfully modified with NAI
746 electrophile. The boxes represent the interquartile range (IQR) of each data-set, with the median value
747 indicated by a line, average value indicated by a “x”. Tukey-style whiskers extend 1.5 x IQR beyond each
748 box. Values outside this range are not shown. ****p<0.0001 by equal variance unpaired student t test.

749

750 **Figure 2.** *De novo* full-length structure prediction of SARS-CoV-2 genomic RNA identifies conserved
751 functional elements at the 5’ and 3’ viral termini. **A)** Consensus structure prediction for the 5’ terminus
752 of SARS-CoV-2, colored by SHAPE Reactivity. Functional domains are labeled, including TRS sequence,
753 start codon of uORF, and start codon of Orf1a (indicated by black, grey, and green lines, respectively).
754 Inset – mapping of SHAPE reactivity data to single- and double-stranded regions, data are plotted with
755 a line indicating the median, and whiskers indicating the standard deviation **B)** Structure prediction for
756 the 3’ terminus of SARS-CoV-2, colored by SHAPE reactivity. Functional domains are labeled. The
757 putative pseudoknot is indicated by solid black lines. Locations of the octanucleotide motif (ONM),
758 hypervariable region (HVR) and S2M are indicated by black lines. Inset – mapping of SHAPE reactivity
759 to single- and double-stranded regions. Data are plotted with a line indicating the median, and
760 whiskers indicating the standard deviation ****p<0.0001 by equal variance unpaired student t test.

761

762 **Figure 3.** Structure prediction of the programmed ribosomal frame-shifting (PRF) element suggests
763 conformational variability of Stem Loop 2. **A)** Dominant PRF structural architecture, predicted by
764 SuperFold, colored by relative SHAPE Reactivity from this study. AS = Attenuator Stem; HSS =

765 Heptanucleotide Slippery Sequence; SL1 = Stem Loop 1; dotted line indicates region reported to form
766 stem loop 2 (SL2) or to form long-range interactions outside the PRF region in the SuperFold prediction;
767 SL3 = Stem Loop 3; Red lines indicate pseudoknot interaction. **B)** Lower probability PRF conformation,
768 with fully-formed SL2, colored by relative SHAPE Reactivity **C)** Dominant PRF structure prediction
769 colored by relative Shannon entropy, labeled as in Panel A. **D)** Base-pairing probability for alternate SL2
770 conformation. Each dot represents a base pair in SL2. A base-pairing probability of 0.25 indicates a
771 25% probability of pairing for the indicated nucleotide.

772

773 **Figure 4.** Full-length genome structure prediction of SARS-CoV-2 Orf1ab reveals a network of well-
774 folded regions. **A)** Analysis of Shannon Entropy and SHAPE reactivities reveals 40 highly structured,
775 well-determined domains in Orf1ab. Nucleotide coordinates are indicated on the x-axis and numbered
776 in 1000 nucleotide intervals. Local median SHAPE reactivity and local median Shannon Entropy are
777 indicated by blue and orange lines, respectively. Well-folded regions are shaded with grey boxes. Arc
778 plots for all base-pairing interactions predicted by the structural model are shown beneath the local
779 SHAPE and Shannon entropy windows, corresponding to the genomic coordinates indicated on the x-
780 axis. The 5'UTR and non-structural protein (Nsp) domains are indicated by colored bars underneath arc
781 plot diagrams. **B)** Representative secondary structure predictions of two regions extracted from the
782 full-length consensus structure generated for the SARS-CoV-2 genome, with Nsp identity and genomic
783 position indicated.

784

785 **Figure 5.** Full-length genome structure prediction of SARS-CoV-2 Orf1ab reveals a unique genome
786 architecture. **A)** Regions encoding individual non-structural protein (Nsp) domains have comparable

787 overall double-stranded RNA content (indicated by grey bars), but they do not adopt equally well-
788 folded substructures (indicated by black bars). A dotted line at 50% nucleotide content has been added
789 for clarity. **B)** SARS-CoV-2 has a shorter median base-pairing distance when compared to median base-
790 pairing distance in previously reported, full-length genome structures for two other positive-sense RNA
791 viruses (Mauger, *et al.*, 2015; Dethoff, *et al.*, 2018). Data are presented in Tukey-style box and
792 whiskers plot as described in Fig. 1B. Asterisk definitions are below. **C)** SARS-CoV-2 has a shorter
793 median base-pairing distance across well-folded regions of RNA when compared to those identified in
794 HIV (Siegfried, *et al.*, 2014). Data are presented as in B). * $p < 0.05$, **** $p < 0.0001$ by equal variance
795 unpaired student t test.

796

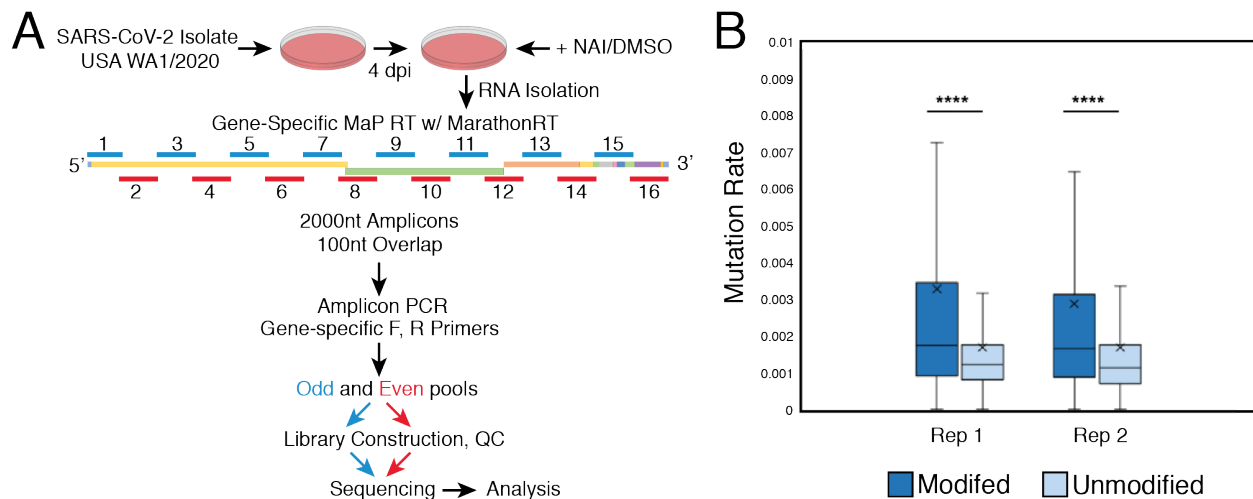
797 **Figure 6.** Structure-dependent variations in synonymous mutation rates suggest that all β -
798 coronaviruses have highly structured genomes (high BPC). **A)** Synonymous mutation rates calculated
799 across all β -coronaviruses for single- and double-stranded nucleotides of Orf1ab. Data are presented in
800 Tukey-style box and whiskers plot as described in Fig. 1B. **B)** Non-synonymous mutation rates
801 calculated across all β -coronaviruses for single- and double-stranded nucleotides of Orf1ab. Data are
802 presented as in (A). **C)** Comparison of synonymous mutation rates for single- and double-stranded
803 nucleotides within individual protein domains, calculated across all β -coronaviruses. Data are
804 presented as in (A). n.s. not significant, * $p < 0.05$, *** $p < 0.001$ **** $p < 0.0001$ by equal variance unpaired
805 student t test.

806

807 **Figure 7.** Analysis of synonymous mutation rates within individual well-folded regions of the SARS-CoV-
808 2 genome identifies four regions that appear to be conserved across β -coronaviruses. **A)** Schematic of

809 well-folded regions in SARS-COV2 genome supported by Synonymous mutation rate analysis in β -
810 coronaviruses. **B)** Synonymous mutation rate separated by stranded-ness in four individual well-folded
811 regions. Data are plotted with a line indicating the median, and whiskers indicating the interquartile
812 range central. * $p < 0.05$, ** $p < 0.01$ by equal variance unpaired student t test. **C), D), E), F)** RNA
813 secondary structure diagrams of four well-folded regions supported by analysis of synonymous
814 mutation rates, colored by SHAPE reactivities, with genomic coordinates indicated below and in (A).
815
816 **Figure 8.** Analysis of synonymous mutation rates and covariation within individual regions of the SARS-
817 CoV-2 genome pinpoints five regions that are conserved only within the sarbecovirus
818 subgenus. **A)** Schematic of well-folded regions in the SARS-COV2 genome supported by Synonymous
819 mutation rate analysis in the sarbecovirus subgenus. **B)** Synonymous mutation rate separated by
820 stranded-ness in five individual well-folded regions. Data are plotted with a line indicating the median,
821 and whiskers indicating the interquartile range central. * $p < 0.05$, ** $p < 0.01$ by equal variance unpaired
822 student t test. **C), D)** RNA secondary structures of two well-folded regions colored by SHAPE
823 reactivity **E), F), G)** RNA secondary structure diagrams of three well-folded regions supported by both
824 synonymous mutation rate analysis and covariation in sarbecoviruses, colored by SHAPE reactivities.
825 Green boxes indicate significant covariation base pairs tested by Rscape-RAFSp(e-value <0.05).
826 Consensus nucleotides are colored by relative degree of sequence conservation within the alignment
827 (75% identity in gray, 90% identify in black, 97% identity in red). Individual nucleotides are represented
828 by circles according to their positional conservation and percentage occupancy thresholds (50%
829 occupancy in white, 75% occupancy in grey, 90% occupancy in black, 97% occupancy in red). Multiple
830 sequence alignment files are provided in supplementary materials.

831 **Figure 1**



832

833

834

835

836

837

838

839

840

841

842

843

844

845

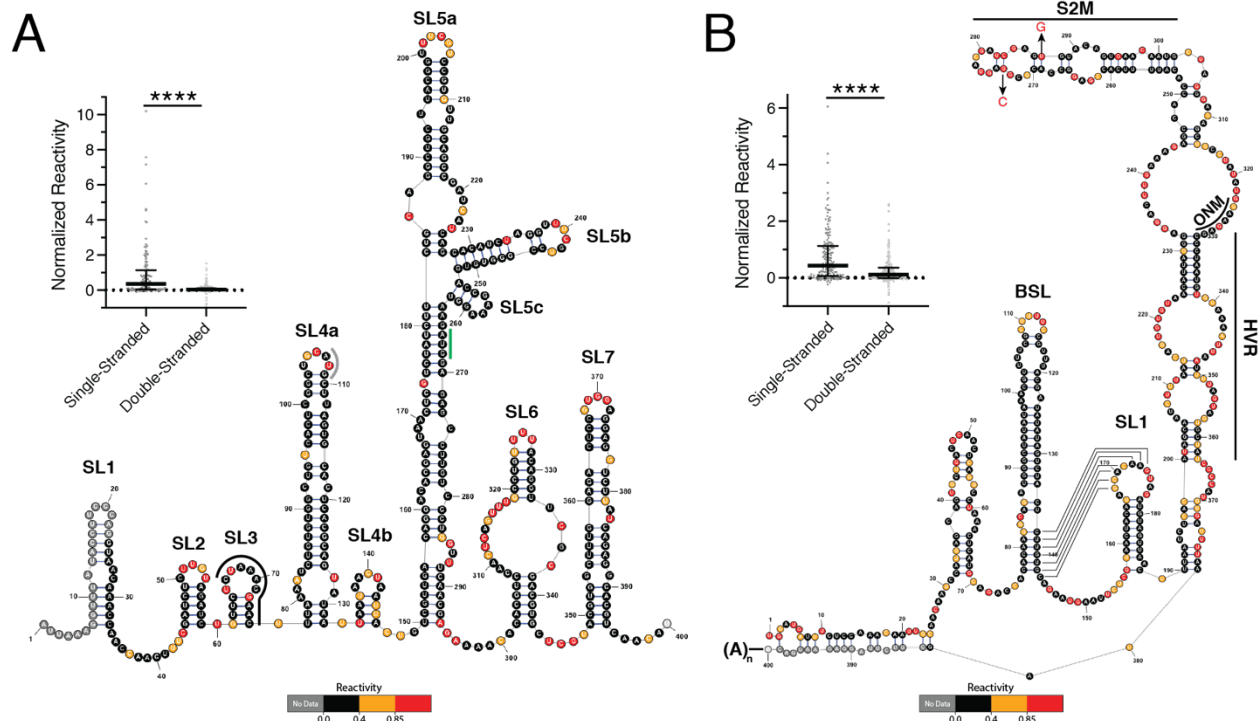
846

847

848

849

850 **Figure 2**



851

852

853

854

855

856

857

858

859

860

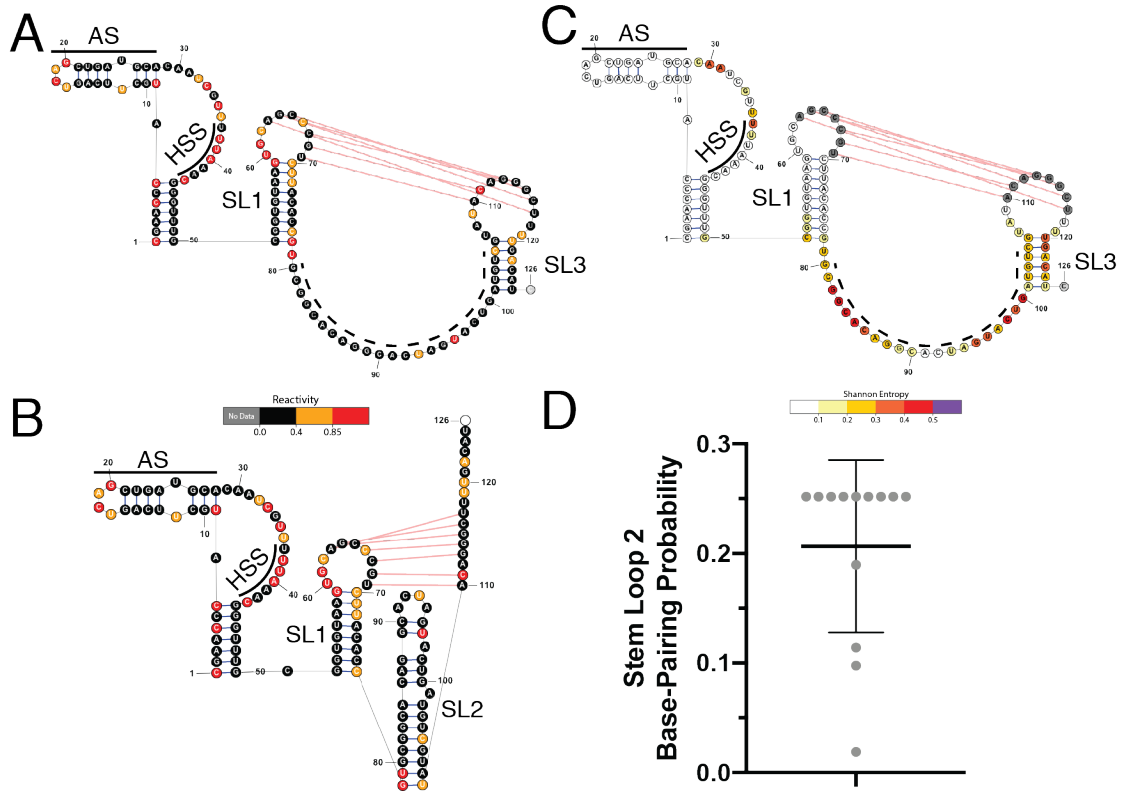
861

862

863

864

865 **Figure 3**



866

867

868

869

870

871

872

873

874

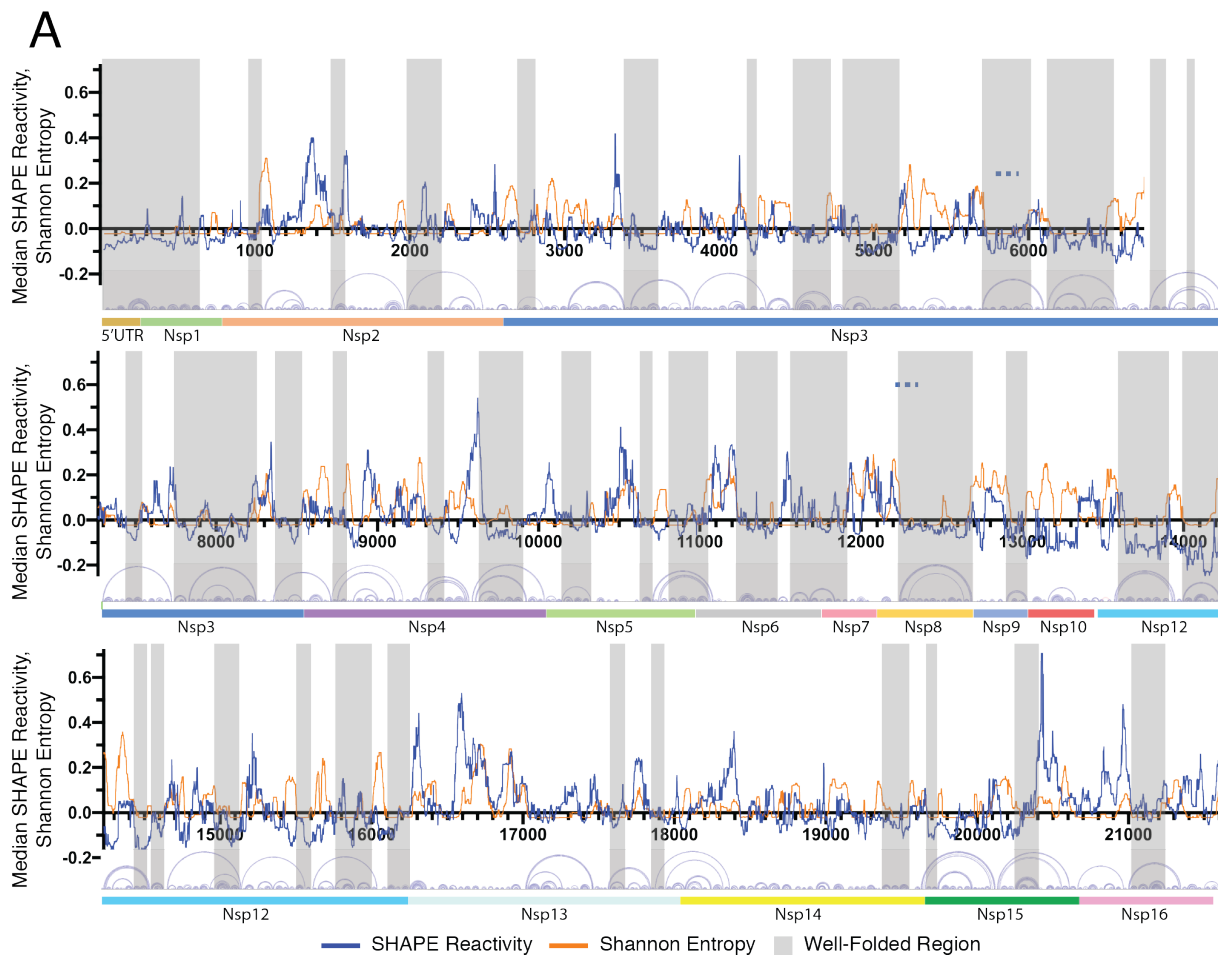
875

876

877

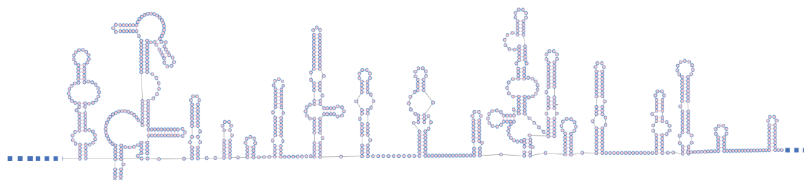
878

879 **Figure 4**

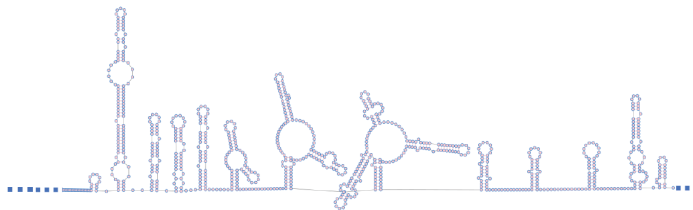


B

Nsp3,
nt 4716 - 5682



Nsp6 - Nsp7
nt 11221 - 12043



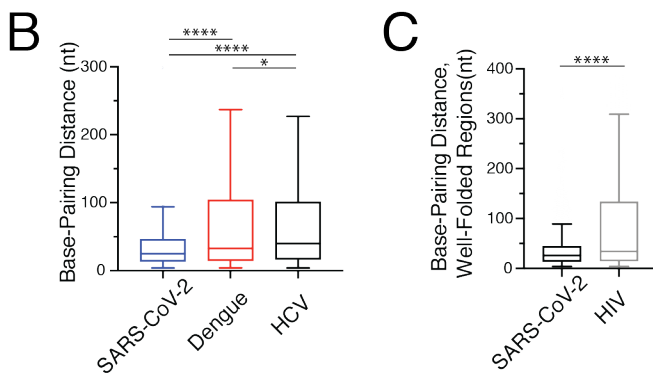
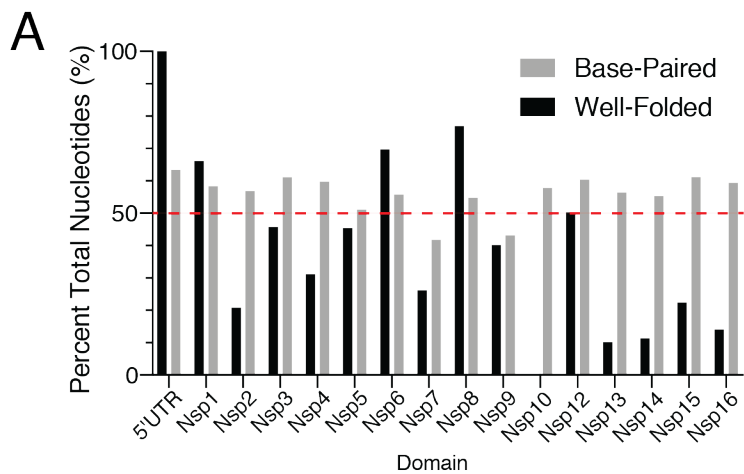
880

881

882

883

884 **Figure 5**



885

886

887

888

889

890

891

892

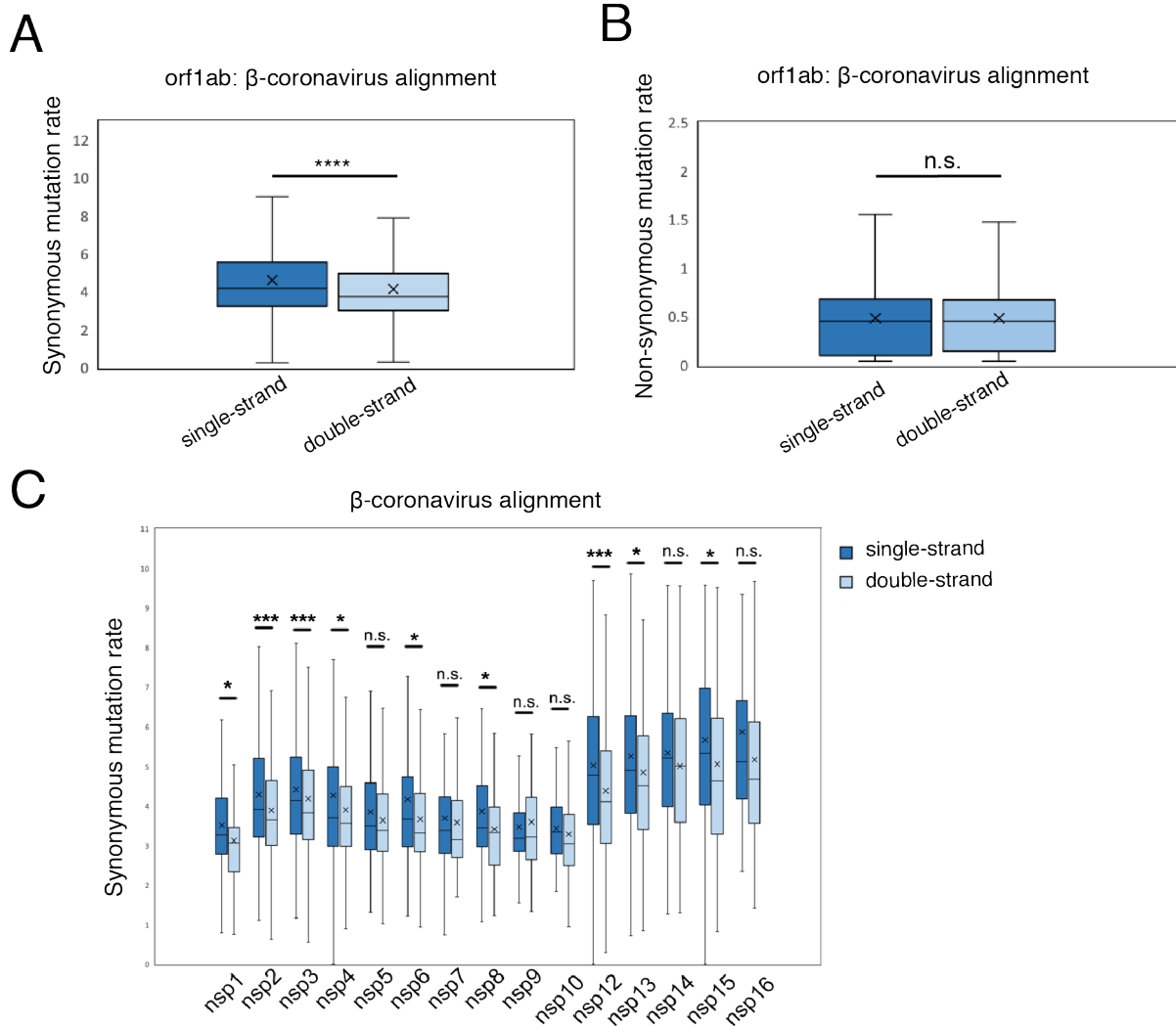
893

894

895

896

897 **Figure 6**



898

899

900

901

902

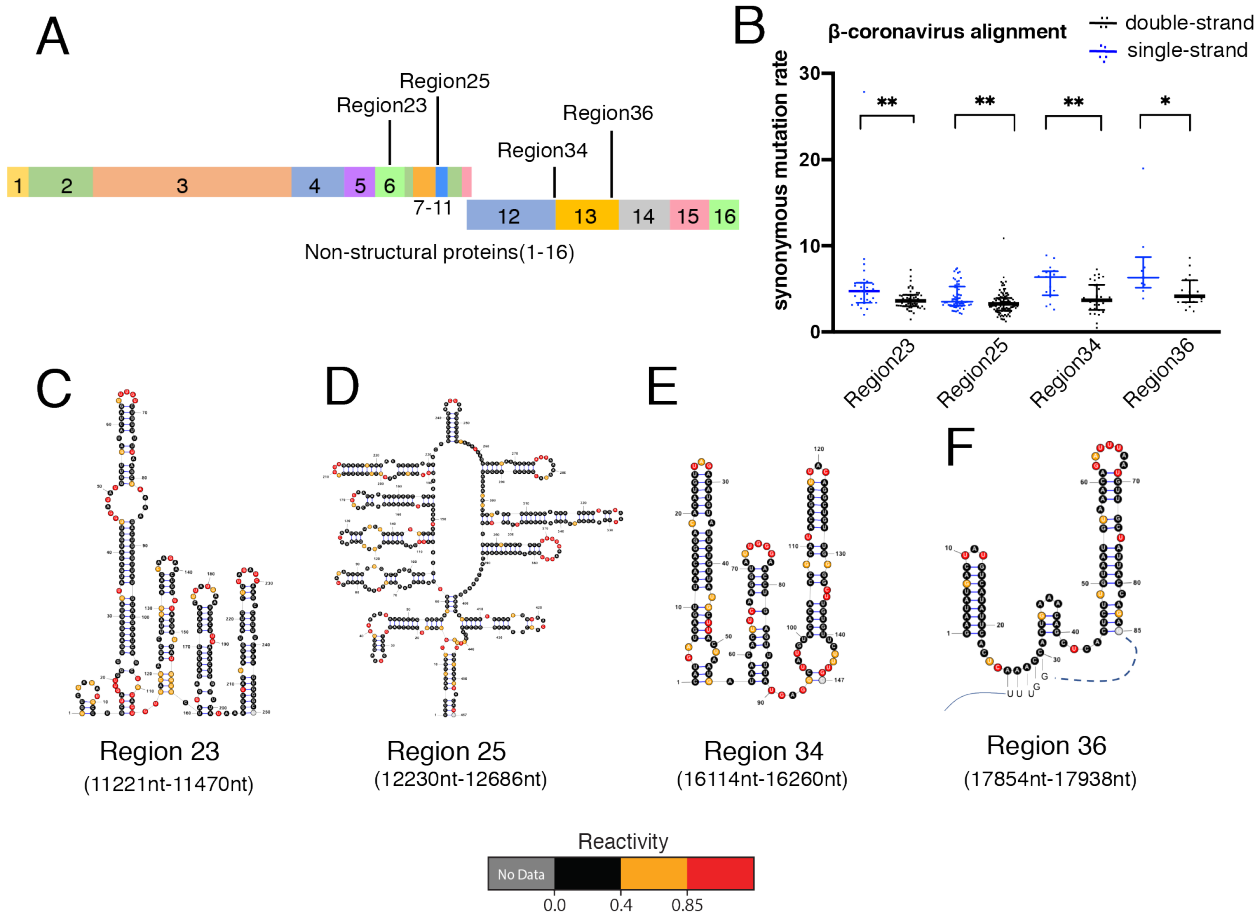
903

904

905

906

907 **Figure 7**



908

909

910

911

912

913

914

915

916

917

918

922 **References**

- 923 ADAMS, R. L., PIRAKITIKULR, N. & PYLE, A. M. 2017. Functional RNA structures throughout the Hepatitis
924 C Virus genome. *Curr Opin Virol*, 24, 79-86.
- 925 ANDREWS, R. J., PETERSON, J. M., HANIFF, H. S., CHEN, J., WILLIAMS, C., GREFE, M., DISNEY, M. D. &
926 MOSS, W. N. 2020. An in silico map of the SARS-CoV-2 RNA Structurome. *bioRxiv*.
- 927 ASSIS, R. 2014. Strong epistatic selection on the RNA secondary structure of HIV. *PLoS Pathog*, 10,
928 e1004363.
- 929 BARANOV, P. V., HENDERSON, C. M., ANDERSON, C. B., GESTELAND, R. F., ATKINS, J. F. & HOWARD, M.
930 T. 2005. Programmed ribosomal frameshifting in decoding the SARS-CoV genome. *Virology*, 332,
931 498-510.
- 932 BARROWS, N. J., CAMPOS, R. K., LIAO, K. C., PRASANTH, K. R., SOTO-ACOSTA, R., YEH, S. C., SCHOTT-
933 LERNER, G., POMPON, J., SESSIONS, O. M., BRADRICK, S. S. & GARCIA-BLANCO, M. A. 2018.
934 Biochemistry and Molecular Biology of Flaviviruses. *Chem Rev*, 118, 4448-4482.
- 935 BENSON, D. A., CAVANAUGH, M., CLARK, K., KARSCH-MIZRACHI, I., OSTELL, J., PRUITT, K. D. & SAYERS,
936 E. W. 2018. GenBank. *Nucleic Acids Res*, 46, D41-D47.
- 937 BUSAN, S. & WEEKS, K. M. 2018. Accurate detection of chemical modifications in RNA by mutational
938 profiling (MaP) with ShapeMapper 2. *RNA*, 24, 143-148.
- 939 CERAOLO, C. & GIORGI, F. M. 2020. Genomic variance of the 2019-nCoV coronavirus. *J Med Virol*, 92,
940 522-528.
- 941 CHEN, C., ZHANG, H., BROITMAN, S. L., REICHE, M., FARRELL, I., COOPERMAN, B. S. & GOLDMAN, Y. E.
942 2013. Dynamics of translation by single ribosomes through mRNA secondary structures. *Nat*
943 *Struct Mol Biol*, 20, 582-8.
- 944 CHEN, S. C. & OLSTHOORN, R. C. 2010. Group-specific structural features of the 5'-proximal sequences
945 of coronavirus genomic RNAs. *Virology*, 401, 29-41.
- 946 CHO, C. P., LIN, S. C., CHOU, M. Y., HSU, H. T. & CHANG, K. Y. 2013. Regulation of programmed
947 ribosomal frameshifting by co-translational refolding RNA hairpins. *PLoS One*, 8, e62283.
- 948 CLYDE, K. & HARRIS, E. 2006. RNA secondary structure in the coding region of dengue virus type 2
949 directs translation start codon selection and is required for viral replication. *J Virol*, 80, 2170-82.
- 950 COLLART, M. A. & WEISS, B. 2020. Ribosome pausing, a dangerous necessity for co-translational events.
951 *Nucleic Acids Res*, 48, 1043-1055.
- 952 DE WIT, E., VAN DOREMALEN, N., FALZARANO, D. & MUNSTER, V. J. 2016. SARS and MERS: recent
953 insights into emerging coronaviruses. *Nat Rev Microbiol*, 14, 523-34.
- 954 DETHOFF, E. A., BOERNEKE, M. A., GOKHALE, N. S., MUHIRE, B. M., MARTIN, D. P., SACCO, M. T.,
955 MCFADDEN, M. J., WEINSTEIN, J. B., MESSER, W. B., HORNER, S. M. & WEEKS, K. M. 2018.
956 Pervasive tertiary structure in the dengue virus RNA genome. *Proc Natl Acad Sci U S A*, 115,
957 11513-11518.
- 958 DIAS JUNIOR, A. G., SAMPAIO, N. G. & REHWINKEL, J. 2019. A Balancing Act: MDA5 in Antiviral
959 Immunity and Autoinflammation. *Trends Microbiol*, 27, 75-85.
- 960 DONG, E., DU, H. & GARDNER, L. 2020. An interactive web-based dashboard to track COVID-19 in real
961 time. *Lancet Infect Dis*, 20, 533-534.
- 962 FEDOROVA, O., JAGDMANN, G. E., JR., ADAMS, R. L., YUAN, L., VAN ZANDT, M. C. & PYLE, A. M. 2018.
963 Small molecules that target group II introns are potent antifungal agents. *Nat Chem Biol*, 14,
964 1073-1078.

- 965 FRICKE, M., DUNNES, N., ZAYAS, M., BARTENSCHLAGER, R., NIEPMANN, M. & MARZ, M. 2015.
966 Conserved RNA secondary structures and long-range interactions in hepatitis C viruses. *RNA*, 21,
967 1219-32.
- 968 FRIEBE, P. & BARTENSCHLAGER, R. 2009. Role of RNA structures in genome terminal sequences of the
969 hepatitis C virus for replication and assembly. *J Virol*, 83, 11989-95.
- 970 GOEBEL, S. J., HSUE, B., DOMBROWSKI, T. F. & MASTERS, P. S. 2004. Characterization of the RNA
971 components of a putative molecular switch in the 3' untranslated region of the murine
972 coronavirus genome. *J Virol*, 78, 669-82.
- 973 GOEBEL, S. J., MILLER, T. B., BENNETT, C. J., BERNARD, K. A. & MASTERS, P. S. 2007. A hypervariable
974 region within the 3' cis-acting element of the murine coronavirus genome is nonessential for
975 RNA synthesis but affects pathogenesis. *J Virol*, 81, 1274-87.
- 976 GUO, L. T., ADAMS, R. L., WAN, H., HUSTON, N. C., POTAPOVA, O., OLSON, S., GALLARDO, C. M.,
977 GRAVELEY, B. R., TORBETT, B. E. & PYLE, A. M. 2020. Sequencing and Structure Probing of Long
978 RNAs Using MarathonRT: A Next-Generation Reverse Transcriptase. *J Mol Biol*, 432, 3338-3352.
- 979 HAJDIN, C. E., BELLAOUSOV, S., HUGGINS, W., LEONARD, C. W., MATHEWS, D. H. & WEEKS, K. M. 2013.
980 Accurate SHAPE-directed RNA secondary structure modeling, including pseudoknots. *Proc Natl
981 Acad Sci U S A*, 110, 5498-503.
- 982 HEWITT, W. M., CALABRESE, D. R. & SCHNEEKLOTH, J. S., JR. 2019. Evidence for ligandable sites in
983 structured RNA throughout the Protein Data Bank. *Bioorg Med Chem*, 27, 2253-2260.
- 984 KANG, H., FENG, M., SCHROEDER, M. E., GIEDROC, D. P. & LEIBOWITZ, J. L. 2006. Putative cis-acting
985 stem-loops in the 5' untranslated region of the severe acute respiratory syndrome coronavirus
986 can substitute for their mouse hepatitis virus counterparts. *J Virol*, 80, 10600-14.
- 987 KELLY, J. A., OLSON, A. N., NEUPANE, K., MUNSHI, S., SAN EMETERIO, J., POLLACK, L., WOODSIDE, M. T.
988 & DINMAN, J. D. 2020. Structural and functional conservation of the programmed -1 ribosomal
989 frameshift signal of SARS coronavirus 2 (SARS-CoV-2). *J Biol Chem*.
- 990 KIM, D., LEE, J. Y., YANG, J. S., KIM, J. W., KIM, V. N. & CHANG, H. 2020. The Architecture of SARS-CoV-2
991 Transcriptome. *Cell*, 181, 914-921 e10.
- 992 KORBIE, D. J. & MATTICK, J. S. 2008. Touchdown PCR for increased specificity and sensitivity in PCR
993 amplification. *Nat Protoc*, 3, 1452-6.
- 994 LAI, D., PROCTOR, J. R., ZHU, J. Y. & MEYER, I. M. 2012. R-CHIE: a web server and R package for
995 visualizing RNA secondary structures. *Nucleic Acids Res*, 40, e95.
- 996 LAN, J., GE, J., YU, J., SHAN, S., ZHOU, H., FAN, S., ZHANG, Q., SHI, X., WANG, Q., ZHANG, L. & WANG, X.
997 2020a. Structure of the SARS-CoV-2 spike receptor-binding domain bound to the ACE2 receptor.
998 *Nature*, 581, 215-220.
- 999 LAN, T. C. T., ALLAN, M., MALSICK, L., KHANDWALA, S., NYEO, S. Y., BATHE, M., GRIFFITHS, A. &
000 ROUSKIN, S. 2020b. Structure of the full SARS-CoV-2 RNA genome in infected cells. *bioRxiv*.
- 001 LEAMY, K. A., ASSMANN, S. M., MATHEWS, D. H. & BEVILACQUA, P. C. 2016. Bridging the gap between
002 in vitro and in vivo RNA folding. *Q Rev Biophys*, 49, e10.
- 003 LEE, C. W., LI, L. & GIEDROC, D. P. 2011. The solution structure of coronaviral stem-loop 2 (SL2) reveals
004 a canonical CUYG tetraloop fold. *FEBS Lett*, 585, 1049-53.
- 005 LI, L., KANG, H., LIU, P., MAKKINJE, N., WILLIAMSON, S. T., LEIBOWITZ, J. L. & GIEDROC, D. P. 2008.
006 Structural lability in stem-loop 1 drives a 5' UTR-3' UTR interaction in coronavirus replication. *J
007 Mol Biol*, 377, 790-803.

- 008 LI, P., WEI, Y., MEI, M., TANG, L., SUN, L., HUANG, W., ZHOU, J., ZOU, C., ZHANG, S., QIN, C. F., JIANG, T.,
009 DAI, J., TAN, X. & ZHANG, Q. C. 2018. Integrative Analysis of Zika Virus Genome RNA Structure
010 Reveals Critical Determinants of Viral Infectivity. *Cell Host Microbe*, 24, 875-886 e5.
- 011 LU, Z. J. & MATHEWS, D. H. 2008. OligoWalk: an online siRNA design tool utilizing hybridization
012 thermodynamics. *Nucleic Acids Res*, 36, W104-8.
- 013 MACFADDEN, A., O'DONOGHUE, Z., SILVA, P., CHAPMAN, E. G., OLSTHOORN, R. C., STERKEN, M. G.,
014 PIJLMAN, G. P., BREDENBEEK, P. J. & KIEFT, J. S. 2018. Mechanism and structural diversity of
015 exoribonuclease-resistant RNA structures in flaviviral RNAs. *Nat Commun*, 9, 119.
- 016 MADHUGIRI, R., KARL, N., PETERSEN, D., LAMKIEWICZ, K., FRICKE, M., WEND, U., SCHEUER, R., MARZ,
017 M. & ZIEBUHR, J. 2018. Structural and functional conservation of cis-acting RNA elements in
018 coronavirus 5'-terminal genome regions. *Virology*, 517, 44-55.
- 019 MAIER, H. J., BICKERTON, E. & BRITTON, P. 2015. *Coronaviruses : methods and protocols*, New York,
020 Humana Press ; Springer.
- 021 MANFREDONIA, I., NITHIN, C., PONCE-SALVATIERRA, A., GHOSH, P., WIRECKI, T., MARINUS, T.,
022 OGANDO, N. S., SNIDER, E. J., VAN HEMERT, M. J., BUJNICKI, J. M. & INCARNATO, D. 2020.
023 Genome-wide mapping of therapeutically-relevant SARS-CoV-2 RNA structures. *bioRxiv*.
- 024 MAUGER, D. M., GOLDEN, M., YAMANE, D., WILLIFORD, S., LEMON, S. M., MARTIN, D. P. & WEEKS, K.
025 M. 2015. Functionally conserved architecture of hepatitis C virus RNA genomes. *Proc Natl Acad
026 Sci U S A*, 112, 3692-7.
- 027 MCMULLAN, L. K., GRAKOU, A., EVANS, M. J., MIHALIK, K., PUIG, M., BRANCH, A. D., FEINSTONE, S. M.
028 & RICE, C. M. 2007. Evidence for a functional RNA element in the hepatitis C virus core gene.
029 *Proc Natl Acad Sci U S A*, 104, 2879-84.
- 030 MITCHELL, D., 3RD, ASSMANN, S. M. & BEVILACQUA, P. C. 2019. Probing RNA structure in vivo. *Curr
031 Opin Struct Biol*, 59, 151-158.
- 032 MURRELL, B., MOOLA, S., MABONA, A., WEIGHILL, T., SHEWARD, D., KOSAKOVSKY POND, S. L. &
033 SCHEFFLER, K. 2013. FUBAR: a fast, unconstrained bayesian approximation for inferring
034 selection. *Mol Biol Evol*, 30, 1196-205.
- 035 NISHIKURA, K. 2010. Functions and regulation of RNA editing by ADAR deaminases. *Annu Rev Biochem*,
036 79, 321-49.
- 037 PIRAKITIKULR, N., KOHLWAY, A., LINDENBACH, B. D. & PYLE, A. M. 2016. The Coding Region of the HCV
038 Genome Contains a Network of Regulatory RNA Structures. *Mol Cell*, 62, 111-20.
- 039 PLANT, E. P. & DINMAN, J. D. 2008. The role of programmed-1 ribosomal frameshifting in coronavirus
040 propagation. *Front Biosci*, 13, 4873-81.
- 041 PLANT, E. P., PEREZ-ALVARADO, G. C., JACOBS, J. L., MUKHOPADHYAY, B., HENNIG, M. & DINMAN, J. D.
042 2005. A three-stemmed mRNA pseudoknot in the SARS coronavirus frameshift signal. *PLoS Biol*,
043 3, e172.
- 044 PLANT, E. P., SIMS, A. C., BARIC, R. S., DINMAN, J. D. & TAYLOR, D. R. 2013. Altering SARS coronavirus
045 frameshift efficiency affects genomic and subgenomic RNA production. *Viruses*, 5, 279-94.
- 046 RAMAN, S., BOUMA, P., WILLIAMS, G. D. & BRIAN, D. A. 2003. Stem-loop III in the 5' untranslated
047 region is a cis-acting element in bovine coronavirus defective interfering RNA replication. *J Virol*,
048 77, 6720-30.
- 049 RANGAN, R., ZHELUEV, I. N. & DAS, R. 2020. RNA genome conservation and secondary structure in
050 SARS-CoV-2 and SARS-related viruses: a first look. *RNA*.

- 051 RANWEZ, V., DOUZERY, E. J. P., CAMBON, C., CHANTRET, N. & DELSUC, F. 2018. MACSE v2: Toolkit for
052 the Alignment of Coding Sequences Accounting for Frameshifts and Stop Codons. *Mol Biol Evol*,
053 35, 2582-2584.
- 054 REGULSKI, E. E. & BREAKER, R. R. 2008. In-line probing analysis of riboswitches. *Methods Mol Biol*, 419,
055 53-67.
- 056 REUTER, J. S. & MATHEWS, D. H. 2010. RNAstructure: software for RNA secondary structure prediction
057 and analysis. *BMC Bioinformatics*, 11, 129.
- 058 RIVAS, E., CLEMENTS, J. & EDDY, S. R. 2017. A statistical test for conserved RNA structure shows lack of
059 evidence for structure in lncRNAs. *Nat Methods*, 14, 45-48.
- 060 ROBERTSON, M. P., IGEL, H., BAERTSCH, R., HAUSSLER, D., ARES, M., JR. & SCOTT, W. G. 2005. The
061 structure of a rigorously conserved RNA element within the SARS virus genome. *PLoS Biol*, 3, e5.
- 062 ROUSKIN, S., ZUBRADT, M., WASHIETL, S., KELLIS, M. & WEISSMAN, J. S. 2014. Genome-wide probing of
063 RNA structure reveals active unfolding of mRNA structures in vivo. *Nature*, 505, 701-5.
- 064 SIEGFRIED, N. A., BUSAN, S., RICE, G. M., NELSON, J. A. & WEEKS, K. M. 2014. RNA motif discovery by
065 SHAPE and mutational profiling (SHAPE-MaP). *Nat Methods*, 11, 959-65.
- 066 SIMMONDS, P. & SMITH, D. B. 1999. Structural constraints on RNA virus evolution. *J Virol*, 73, 5787-94.
- 067 SIMON, L. M., MORANDI, E., LUGANINI, A., GRIBAUDO, G., MARTINEZ-SOBRIDO, L., TURNER, D. H.,
068 OLIVIERO, S. & INCARNATO, D. 2019. In vivo analysis of influenza A mRNA secondary structures
069 identifies critical regulatory motifs. *Nucleic Acids Res*, 47, 7003-7017.
- 070 SMOLA, M. J., CALABRESE, J. M. & WEEKS, K. M. 2015a. Detection of RNA-Protein Interactions in Living
071 Cells with SHAPE. *Biochemistry*, 54, 6867-75.
- 072 SMOLA, M. J., CHRISTY, T. W., INOUE, K., NICHOLSON, C. O., FRIEDERSDORF, M., KEENE, J. D., LEE, D. M.,
073 CALABRESE, J. M. & WEEKS, K. M. 2016. SHAPE reveals transcript-wide interactions, complex
074 structural domains, and protein interactions across the Xist lncRNA in living cells. *Proc Natl Acad
075 Sci U S A*, 113, 10322-7.
- 076 SMOLA, M. J., RICE, G. M., BUSAN, S., SIEGFRIED, N. A. & WEEKS, K. M. 2015b. Selective 2'-hydroxyl
077 acylation analyzed by primer extension and mutational profiling (SHAPE-MaP) for direct,
078 versatile and accurate RNA structure analysis. *Nat Protoc*, 10, 1643-69.
- 079 TAVARES, R., MAHADESHWAR, G. & PYLE, A. M. 2020. The global and local distribution of RNA
080 structure throughout the SARS-CoV-2 genome. *bioRxiv*.
- 081 TAVARES, R. C. A., PYLE, A. M. & SOMAROWTHU, S. 2019. Phylogenetic Analysis with Improved
082 Parameters Reveals Conservation in lncRNA Structures. *J Mol Biol*, 431, 1592-1603.
- 083 TUPLIN, A., WOOD, J., EVANS, D. J., PATEL, A. H. & SIMMONDS, P. 2002. Thermodynamic and
084 phylogenetic prediction of RNA secondary structures in the coding region of hepatitis C virus.
085 *RNA*, 8, 824-41.
- 086 VAN TREECK, B., PROTTER, D. S. W., MATHENY, T., KHONG, A., LINK, C. D. & PARKER, R. 2018. RNA self-
087 assembly contributes to stress granule formation and defining the stress granule transcriptome.
088 *Proc Natl Acad Sci U S A*, 115, 2734-2739.
- 089 WAN, Y., KERTESZ, M., SPITALE, R. C., SEGAL, E. & CHANG, H. Y. 2011. Understanding the transcriptome
090 through RNA structure. *Nat Rev Genet*, 12, 641-55.
- 091 WAN, Y., SHANG, J., GRAHAM, R., BARIC, R. S. & LI, F. 2020. Receptor Recognition by the Novel
092 Coronavirus from Wuhan: an Analysis Based on Decade-Long Structural Studies of SARS
093 Coronavirus. *J Virol*, 94.

- 094 WARNER, K. D., HAJDIN, C. E. & WEEKS, K. M. 2018. Principles for targeting RNA with drug-like small
095 molecules. *Nat Rev Drug Discov*, 17, 547-558.
- 096 WATERHOUSE, A. M., PROCTER, J. B., MARTIN, D. M., CLAMP, M. & BARTON, G. J. 2009. Jalview
097 Version 2--a multiple sequence alignment editor and analysis workbench. *Bioinformatics*, 25,
098 1189-91.
- 099 YANG, D. & LEIBOWITZ, J. L. 2015. The structure and functions of coronavirus genomic 3' and 5' ends.
100 *Virus Res*, 206, 120-33.
- 101 YANG, D., LIU, P., WUDECK, E. V., GIEDROC, D. P. & LEIBOWITZ, J. L. 2015. SHAPE analysis of the RNA
102 secondary structure of the Mouse Hepatitis Virus 5' untranslated region and N-terminal nsp1
103 coding sequences. *Virology*, 475, 15-27.
- 104 YIN, W., MAO, C., LUAN, X., SHEN, D. D., SHEN, Q., SU, H., WANG, X., ZHOU, F., ZHAO, W., GAO, M.,
105 CHANG, S., XIE, Y. C., TIAN, G., JIANG, H. W., TAO, S. C., SHEN, J., JIANG, Y., JIANG, H., XU, Y.,
106 ZHANG, S., ZHANG, Y. & XU, H. E. 2020. Structural basis for inhibition of the RNA-dependent
107 RNA polymerase from SARS-CoV-2 by remdesivir. *Science*, 368, 1499-1504.
- 108 YOU, S., STUMP, D. D., BRANCH, A. D. & RICE, C. M. 2004. A cis-acting replication element in the
109 sequence encoding the NS5B RNA-dependent RNA polymerase is required for hepatitis C virus
110 RNA replication. *J Virol*, 78, 1352-66.
- 111 ZHU, N., ZHANG, D., WANG, W., LI, X., YANG, B., SONG, J., ZHAO, X., HUANG, B., SHI, W., LU, R., NIU, P.,
112 ZHAN, F., MA, X., WANG, D., XU, W., WU, G., GAO, G. F., TAN, W., CHINA NOVEL CORONAVIRUS,
113 I. & RESEARCH, T. 2020. A Novel Coronavirus from Patients with Pneumonia in China, 2019. *N*
114 *Engl J Med*, 382, 727-733.
- 115 ZUBRADT, M., GUPTA, P., PERSAD, S., LAMBOWITZ, A. M., WEISSMAN, J. S. & ROUSKIN, S. 2017. DMS-
116 MaPseq for genome-wide or targeted RNA structure probing in vivo. *Nat Methods*, 14, 75-82.
- 117 ZUST, R., MILLER, T. B., GOEBEL, S. J., THIEL, V. & MASTERS, P. S. 2008. Genetic interactions between an
118 essential 3' cis-acting RNA pseudoknot, replicase gene products, and the extreme 3' end of the
119 mouse coronavirus genome. *J Virol*, 82, 1214-28.
- 120